

Learning Interpretable Models Through Multi-Objective NAS

Zachariah Carmichael^{1,2} Tim Moon² Sam Ade Jacobs²

¹University of Notre Dame ²Lawrence Livermore National Laboratory

zcarmich@nd.edu {moon13, jacobs32}@llnl.gov

Abstract

Monumental advances in deep learning have led to unprecedented achievements across various domains. While the performance of deep neural networks is indubitable, the architectural design and interpretability of such models are nontrivial. Research has been introduced to automate the design of neural network architectures through neural architecture search (NAS). Recent progress has made these methods more pragmatic by exploiting distributed computation and novel optimization algorithms. However, there is little work in optimizing architectures for interpretability. To this end, we propose a multi-objective distributed NAS framework that optimizes for both task performance and “introspectability,” a surrogate metric for aspects of interpretability. We leverage the non-dominated sorting genetic algorithm (NSGA-II) and explainable AI (XAI) techniques to reward architectures that can be better comprehended by domain experts. The framework is evaluated on several image classification datasets. We demonstrate that jointly optimizing for task error and introspectability leads to more disentangled and debuggable architectures that perform within tolerable error.

1. Introduction

The success of deep learning is seemingly ubiquitous in a multitude of domains. A core component of its effectiveness is its ability to automate the feature engineering process. Under this perspective, a natural next step is the automation of the architecture design. To this end, *neural architecture search* (NAS) [18] has been proposed. Progress in NAS has led to results that supersede the state-of-the-art in several applications, such as image classification [39] and object detection [50].

While NAS has been effective in automating architecture discovery and topping leaderboards, little attention has been paid to the discovery of interpretable architectures. The automation of interpretability would further minimize the need for “human-in-the-loop” pipelines. Not only does this reduce the manual design needed to meet the constraints of

an application, but it also enhances the comprehensibility of the discovered models. Increased comprehensibility aids in model debugging, decreases time to deployment, and instills greater trust.

Unfortunately, there is a trade-off between increased interpretability and accuracy that bears a point at which the degradation in model quality cannot be justified. A method to quantify these trade-offs would be of great importance to NAS endeavors. Furthermore, the acceptable compromise between these metrics will vary between applications – consider the accuracy needed in biometrics, the explainability required for scientific discovery, and the combination required for medical diagnoses. To this end, we introduce a framework for the joint optimization of task performance and a surrogate for interpretability. In this work, we put forth the following contributions:

- We develop a new metric to quantify interpretability as the disentanglement between latent representations for different data classes: *introspectability*. We further extend this metric by exploiting hierarchical semantic information from the WordNet database.
- We propose a multi-objective evolutionary approach to NAS, *eXplainable NAS* (XNAS), that maximizes both accuracy and introspectability by directly optimizing the Pareto frontier.
- We conduct analyses of the accuracy-introspectability trade-off, explore phylogenetic trees to understand the inheritability of objectives, visualize disentangled representations, analyze architectural motifs along the Pareto front, and demonstrate introspectability as a surrogate for trustworthiness and debuggability.

2. Background & Related Work

Our work is at the intersection of neural architecture search, explainable AI (XAI), evolutionary algorithms, and multi-objective optimization. We present a brief overview of these topics and discuss related work to put our contributions in context.

Neural Architecture Search (NAS) Akin to how deep learning is used to automate feature engineering, NAS al-

gorithms automate *architectural engineering* [18]. NAS algorithms can generally be understood as the composition of three elements: (i) a *search space* that defines the possible neural architectures, (ii) a *search strategy* that explores a search space for candidate solutions, and (iii) a *performance estimation strategy* that determines the fitness of a solution. Of the many approaches to NAS, Bayesian optimization (BO), reinforcement learning (RL), and evolutionary algorithms are the most common. While BO is typically applied to low-dimensional problems, several works have applied it to NAS [5, 14] and it has even surpassed human experts on competition datasets [35]. However, BO has mostly been overshadowed by RL ever since Zoph and Le achieved unprecedented results on NAS benchmarks [49]. The RL problem can be formulated with the evolutionary search space as the agent’s action space and the test set error as the reward [49, 50]. Alternatively, the RL problem can be posed as a sequential control task [7, 44]: given the state of the architecture, what network modification should be applied to improve performance?

While RL-based NAS has achieved state-of-the-art across many benchmarks, it tends to be compute-inefficient and can take thousands of GPU hours to converge [40, 50]. *Neuro-evolutionary* approaches are generally lightweight in comparison, and they notably perform the same as RL approaches on NAS benchmarks [39]. The use of evolutionary algorithms for NAS can be traced back decades, e.g. [37] uses genetic algorithms to propose architectures that are then trained using backpropagation. While evolutionary algorithms have been used to search for both weights and network architectures [2, 43], it is more common to only apply evolution to the architecture and to train the weights with gradient descent [17, 39, 40]. Evolutionary algorithms evolve a population of candidate solutions to an optimization problem and each generation is derived from the last by applying mating operations to a set of selected parents. In NAS, an offspring may differ from its parents by an added layer, a changed connection, etc. The quality of solutions is judged by a fitness function and evolution is terminated when a resource or time budget is exceeded.

Multi-Objective Optimization & NAS In a multi-objective optimization problem, there are m objectives $\{f_1, \dots, f_m\}$, which in the context of NAS may be accuracy, floating point operations (FLOPs), energy, etc. When $m > 1$, it becomes nontrivial to select the optimal solution among the set of all objective vectors $Y = \{\mathbf{y} \in \mathbb{R}^m \mid \mathbf{y} = \{f_1(\mathbf{x}), \dots, f_m(\mathbf{x})\}\}$ where \mathbf{x} is a candidate solution. There exists a variety of strategies to select solutions, such as optimizing for a weighted sum of the (normalized) objectives, lexicographic sorting, or maintaining Pareto-optimal solutions [34]. We are most interested in the latter approach since it captures the trade-offs between objectives and

allows the practitioner to choose the optimal compromise for their use case. The set of Pareto-optimal solutions, also called the Pareto frontier or Pareto front, is the set of non-dominated solutions $\{\mathbf{y}' \in Y \mid \{\mathbf{y} \in Y \mid \mathbf{y} \succ \mathbf{y}'\} = \emptyset\}$, where $\mathbf{a} \succ \mathbf{b}$ indicates that \mathbf{a} strictly dominates \mathbf{b} , i.e. $|\{f_i(\mathbf{a}) \mid 1 \leq i \leq m, f_i(\mathbf{a}) > f_i(\mathbf{b})\}| = m$.

The non-dominated sorting genetic algorithm-II (NSGA-II) [9] is an elitist evolutionary approach to multi-objective optimization. Notably, the authors improve the non-dominated sorting algorithm from cubic to quadratic time complexity. The surviving members of a generation are selected in a binary tournament with preference given to members of the Pareto front. Additional offspring are generated from members in the ranked fronts, i.e. the Pareto fronts computed iteratively after removing the members of the previous front. When a ranked front needs to be sub-sampled, the crowding distance within the front is used to ensure the full front is represented.

Related to our work, NSGA-Net [33] is an evolutionary framework for NAS that employs NSGA-II for multi-objective optimization. Like most evolutionary NAS algorithms, NSGA-Net explores and exploits the search space with a fixed-size population of candidate architectures. These architectures, encoded as a sequence of phases, are initialized either randomly or seeded from hand-crafted architectures like ResNet. In the *exploration* stage, homogeneous crossover and bit-flipping mutation operators are applied to the population to create new offspring. In the *exploitation* stage, Bayesian optimization is used to exploit correlations in architecture blocks over previous trials. NSGA-Net is evaluated on CIFAR-10 and CIFAR-100 with a search space similar to DARTS [31] using two metrics: classification error and computational complexity (FLOPs). The authors demonstrate the effectiveness of population-based NAS and the superiority of NSGA-II over a weighted sum of objectives. While similar to our framework, our focus is on the design of objectives conducive to interpretability. Furthermore, we scale our method to a distributed cluster using Ray [38] and evaluate on more datasets.

Multi-objective optimization of a weighted sum of objectives has been employed by many NAS works. The approach is attractive when the objectives are differentiable since it is amenable to gradient descent by backpropagation. For instance, Multi-Objective NAS (MONAS) [26] uses RL with a weighted combination of accuracy, power, and multiply-accumulate operations (MACs) as the reward. However, there are limitations to optimizing for an aggregate of multiple objectives: it relies on manually tuned coefficients, struggles to accommodate objectives that range over multiple orders of magnitude, and tends to cluster in a small region of the Pareto front.

Explainable AI (XAI) & NAS Some of the intersection between interpretability and NAS has been covered in prior work. In [41], a NAS framework using the Bayesian optimization search strategy is proposed. For efficiency and interpretability, a Weisfeiler-Lehman graph kernel is used to define a Gaussian process surrogate on the search space, and the gradients are used to identify key motifs that lead to well-performing architectures. Similarly, [1, 47] use alternative techniques to identify key motifs used in the search process. However, their notions of interpretability and disentanglement focus on the search process rather than on the learned models themselves. In this work, we extend NAS to disentangle the latent space of learned models.

3. Proposed Framework: XNAS

Following the taxonomy in [18], we break up our method into a search space, search strategy, and performance estimation strategy. We further discuss how we scale the search up to an arbitrary number of compute nodes.

3.1. Search Space

We are interested in exploring complex search spaces beyond simple chains, i.e. multi-branch networks such as ResNet [23] or DenseNet [27]. To this end, we elect to use the popular NAS-Bench-201 search space [16], which is comprised of a macro skeleton and a searched cell. An overview is shown in the supplemental material.

The first layer of the macro skeleton is a 3×3 convolutional layer with $F = 16$ filters followed by a batch normalization layer. This is followed by a stack of five searched cells ($F = 16$). A basic residual block ($F = 32$) with a stride of two proceeds the stacked cell block. The shortcut connection is a 2×2 2D average pooling layer followed by a 1×1 convolutional layer. These blocks are alternated, cutting the image dimensions in half and doubling the filters for each set of blocks. The end of the network is a 2D global average pooling layer followed by a fully-connected (dense) classification layer with a softmax activation.

The searched cell can be expressed as a directed acyclic graph where nodes represent data and edges represent operations. The set of operations consists of 3×3 convolutional blocks, 1×1 convolutional blocks, 3×3 average pooling, “zeroize” (equivalent to dropping the edge), and “skip-connect” (equivalent to the identity operator). Note that each convolutional block is comprised of convolution, a rectified linear (ReLU) activation, and batch normalization. All of the convolutions and pooling layers use SAME padding. To prevent cycles, each node is assigned a rank and can only connect to higher-rank nodes. Since there are $V = 4$ nodes in a cell and five operation candidates in the operation set, the total size of the search space is $5^{\sum_{i=0}^{V-1} i} = 15,625$ architectures. There are two issues with the search space definition, which the NAS-Bench-201

authors also point out. First, different architecture encodings can result in the same graph. Like the authors, we do not consider isomorphism in the evaluation of architectures¹. Second, architectures can be disconnected due to the zeroize operation. In this case, the mating operations are reapplied to produce valid offspring.

We represent an architecture in the search space as \mathbf{x}_i , a fixed-size list of integers of size $\sum_{i=0}^{V-1} i = 6$ with each element in the range $[1..V]$. Each element of this *encoding* represents (i) a specific operator or operators, such as a convolutional or max pooling layer with specific parameters (e.g. kernel size, strides, etc.), or the lack of an operator (identity) and (ii) how that operator is connected to additional operators in the computational graph.

3.2. Search Strategy

As we are interested in discovering neural architectures that are both accurate and interpretable, we propose to use multi-objective optimization. We explore and exploit the search space using the Non-Dominated Sorting Genetic Algorithm II (NSGA-II), as introduced in Section 2, with two objectives: accuracy and *introspectability* (introduced in Section 3.3). Because we search for architectures that are both accurate and interpretable, we refer to our approach as eXplainable NAS (XNAS). We generate the initial set of solutions by uniformly sampling each of the 6 variables in the optimization problem (as defined in Section 3.1). These candidates comprise the first generation of the *population*. Thereafter, the offspring of the proceeding generation are produced by mating the parents comprising the prior generation. Parents are selected based on the ranked Pareto fronts of the population as described in Section 3.3 and [9]. Because of this selection, there is no notion of a single best solution, but rather a set of non-dominated solutions that characterize the optimal trade-off between all objectives.

Mating comprises two core operations: crossover and mutation. The *crossover* operator produces offspring by combining the encodings of two parents. The operator combines the building blocks between successful parents to exploit the *implicit parallelism* of population-based search [25]. Due to the integer-based encoding that we employ in this work, we elect to use simulated binary crossover [10], which uses a probability density function to simulate the single-point crossover of binary-coded genetic algorithms. The *mutation* operator produces offspring by modulating one or more of the variables of a single parent. We specifically select polynomial mutation, which follows the same probability distribution as simulated binary crossover. Both crossover and mutation also have a parameter p that controls the probability that the respective oper-

¹The NAS-Bench-201 authors remark that there are 6,466 architectures with unique topology in the search space due to isomorphisms brought about by the “skip-connect” and “zeroize” operations.

ator is applied to a member of the population.

3.3. Performance Evaluation Strategy

We evaluate the performance of an architecture using two objectives: task performance and interpretability. The former is simple to define quantitatively as the classification accuracy on the held-out validation split of a dataset. However, interpretability is often treated far more qualitatively and an objective definition eludes community consensus. Furthermore, explaining a model is dependent on the audience, data modality, modeling task, and questions being asked. To disambiguate interpretability in the context of the framework, we state our assumptions: that the user has some technical understanding (e.g. a data scientist or domain expert), that we are interested in understanding the model in classification tasks (e.g. as opposed to the data or the NAS evolution process), and that models that maximize the metric lead to qualitatively discernible trends. To this end, we propose to quantify the interpretability of models as the introspectability of disentangled elements, which we describe in the subsequent subsections. We measure this for supervised classification tasks using the pairwise distances between latent representations of individual classes.

Introspectability Here we formalize the score that we denote as *introspectability*: the degree to which the representations of disparate classes within a neural network \mathcal{M} are disentangled. Let us denote the subset of validation data belonging to class c as $\mathcal{X}^{(c)} \in \mathbb{R}^{N^{(c)} \times H \times W \times C}$. Given $\mathcal{X}^{(c)}$ as input to \mathcal{M} , denote the activations of layer l as $\Phi^{(c,l)} \in \mathbb{R}^{N^{(c)} \times d_1^{(l)} \times \dots \times d_n^{(l)}}$. We reshape the activations to have a single dimension of size $d^{(l)} = \prod_{i=1}^n d_i^{(l)}$ such that $\Phi^{(c,l)} \in \mathbb{R}^{N^{(c)} \times d^{(l)}}$. We denote all activations for class c within \mathcal{M} as $\Phi^{(c)} = \parallel_{l=1}^L \Phi^{(c,l)}$ where \parallel is the matrix concatenation operator along the columns and L is the number of layers in \mathcal{M} . The mean activations for class c are then $\bar{\Phi}^{(c)} = \frac{1}{N^{(c)}} \sum_{i=1}^{N^{(c)}} \Phi_i^{(c)}$ where $|\bar{\Phi}^{(c)}| = \sum_{l=1}^L d^{(l)}$. With these definitions, we then formulate introspectability as (1)

$$\text{Introspectability}(\mathcal{M}, \mathcal{X}) = \frac{1}{\binom{N_C}{2}} \sum_{c=1}^{N_C} \sum_{k=c+1}^{N_C} D(\bar{\Phi}^{(c)}, \bar{\Phi}^{(k)}) \quad (1)$$

where $D(\cdot, \cdot)$ gives the cosine distance between its two vector arguments and N_C is the number of classes in the classification task.

Introspectability and WordNet We derive a second definition of introspectability based on WordNet [36], a lexical database of the English language. WordNet comprises sets of synonyms (*synsets*) and arises into a hierarchical representation by embedding the transitive relations *hyponyms* (more specific sub-names) and *hypernyms* (more abstract

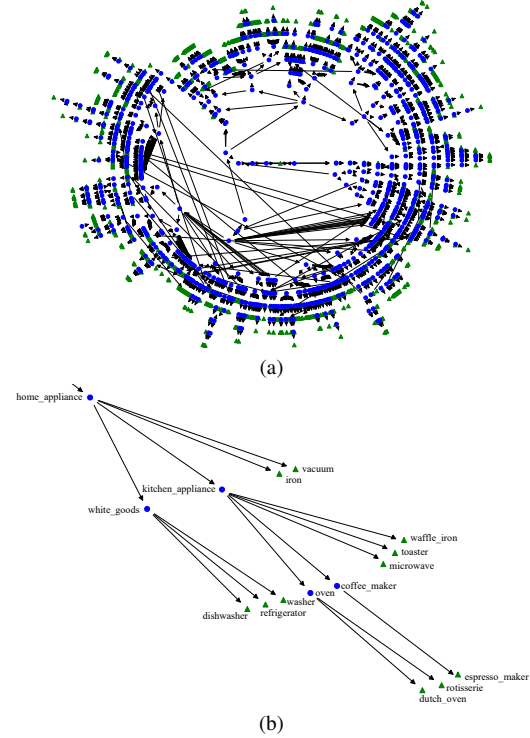


Figure 1. (a) The WordNet hyponym-hypernym graph where leaf nodes (green) are the labels of the ImageNet dataset. (b) An inset of the full graph containing the synset “home appliance” and its hypernyms.

super-names). In computer vision, the labels of the ImageNet database [12] are notably derived from WordNet synsets. We visualize all of the labels covered by ImageNet in the hyponym-hypernym graph shown in Figure 1a and 1b. The shortest path distances between two labels in the hyponym-hypernym graph can be used to compute semantic similarity as shown in (2)

$$\text{path_sim}(w_a, w_b) = \frac{1}{\text{shortest_path}(w_a, w_b) + 1} \quad (2)$$

where w_a and w_b are label names. We then weigh the pairwise distances between classes by this similarity as (3)

$$\text{Introspectability}_{\text{WordNet}}(\mathcal{M}, \mathcal{X}) = \frac{1}{\binom{N_C}{2}} \sum_{c=1}^{N_C} \sum_{k=c+1}^{N_C} D(\bar{\Phi}^{(c)}, \bar{\Phi}^{(k)}) \times S(c, k). \quad (3)$$

The similarity between labels S is given by (4)

$$S(c, k) = \text{path_sim}(\text{name}(c), \text{name}(k)) \quad (4)$$

where $\text{name}(\cdot)$ maps the label index to the corresponding label name. Intuitively, the score penalizes models with rel-

Dataset	Multi-Objective	Gen.	Population-Level Statistics				Hypervolume
			Maximum Accuracy	Median Accuracy	Maximum Intros.	Median Intros.	
MNIST	reg	–	98.9%	98.6%	0.384	0.291	0.341
	✗	18	99.1%	98.8%	0.353	0.255	0.314
	✓	18	99.1%	98.6%	0.390	0.258	0.347
	✓+reg	18	99.0%	98.6%	0.503	0.303	0.424
CIFAR-10	reg	–	85.9%	72.8%	0.331	0.178	0.229
	✗	34	87.7%	84.3%	0.328	0.077	0.237
	✓	34	87.9%	74.6%	0.552	0.196	0.293
	✓+reg	34	87.7%	74.2%	0.654	0.249	0.361
ImageNet-16-120	reg	–	44.8%	36.2%	0.318	0.087	0.099
	✗	11	47.8%	44.9%	0.301	0.053	0.099
	✓	11	47.3%	39.1%	0.317	0.104	0.111
	✓+reg	11	47.4%	39.0%	0.380	0.109	0.117

Table 1. XNAS experimental results on image classification datasets listing the population-level accuracy and introspectability (Intros.) scores, and hypervolume. The regularization term is denoted as “reg” and is described in Section 4.3. Normalized Introspectability_{WordNet} is shown for ImageNet-16-120. Multi-objective XNAS with regularization yields the greatest hypervolume across all tasks.

actively small distances between dissimilar labels and compensates for small distances between similar labels. To ensure the range of WordNet introspectability is comparable to that of the baseline definition, we normalize the score by dividing by the mean `path_sim` value among all pairs of labels in the dataset.

3.4. Scaling Up

We scale XNAS to clusters comprising an arbitrary number of compute nodes using the distributed framework, Ray [38]. Given a set of M nodes $\{n_i\}_{i=1}^M$, n_1 is treated as a head node that is responsible for running the core NSGA-II optimization loop and the core Ray server. The remaining nodes $\{n_i\}_{i=2}^M$ are configured as workers available to train and evaluate architectures on a dataset. When a new generation of architectures is created, each offspring is submitted for fitness evaluation to a queue by the head node. Each job in the queue is offloaded to a free worker until all workers complete their jobs and the queue is empty. The head node n_1 also is treated as an additional worker if it has free resources. Each worker node can execute in parallel as many jobs as it has GPUs.

4. Experiments & Results

We evaluate XNAS on three image classification datasets: MNIST, CIFAR-10, and ImageNet-16-120 [16]. Thereafter, we conduct analyses to understand the evolution process of XNAS, characterize the Pareto front of each task, and demonstrate the debuggability of higher-introspectability architectures.

4.1. Setup and Implementation

The experimental setup and all hyperparameters are detailed in Appendix B. We implement XNAS in Python with code built on the `pymoo` [6], `DeepHyper` [3], and `Ray` [38] libraries. The source code is publicly available at <redacted>.

4.2. Metrics

To quantitatively assess the quality of the solutions from a multi-objective search algorithm, we look to *hypervolume* as introduced in [48] and improved in [20]. Hypervolume can be perceived as the area of the union of rectangles where each rectangle is formed by a point on the Pareto front and a reference point (such as $(0, 0)$). This notion can easily be extended to higher dimensions, i.e. rectangular cuboids are formed with three objectives and hyperrectangles are formed with four or more objectives. In this work, we set the reference point to $(0, 1/N_C)$ where $1/N_C$ is the classification rate of random guessing with balanced data. Note that this reduces the hypervolume range from $[0, 1]$ to $[0, (1-1/N_C)]$. We are interested in setting the reference point here to avoid rewarding models that have not learned the task in any significant capacity.

4.3. Results

Table 1 contains the aggregate results for each task and demonstrates the efficacy of using the proposed multi-objective approach. XNAS is compared with the single-objective NAS baseline. While the median population-level accuracy falls slightly compared to single-objective NAS, the maximum accuracy is still comparatively high and there is a substantial increase in hypervolume across experiments.

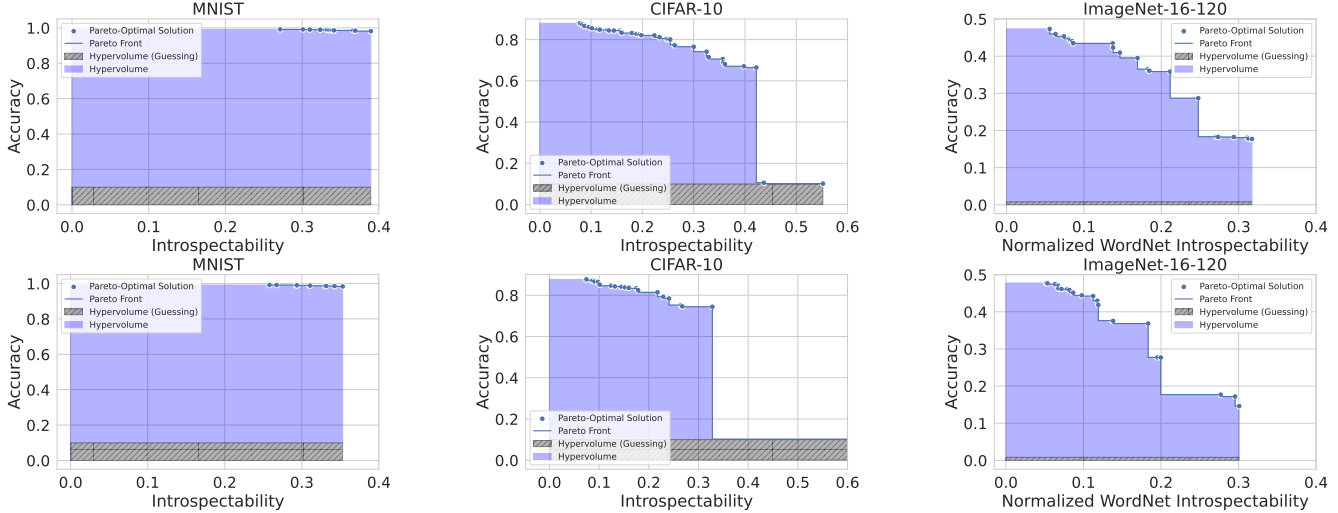


Figure 2. The Pareto fronts and Pareto-optimal solutions are shown for each task. The shaded region visualizes the hypervolume achieved by XNAS. In the first row, the front is visualized for multi-objective XNAS and for single-objective (accuracy only) in the second row. Normalized Introspectability_{WordNet} is shown for ImageNet-16-120.

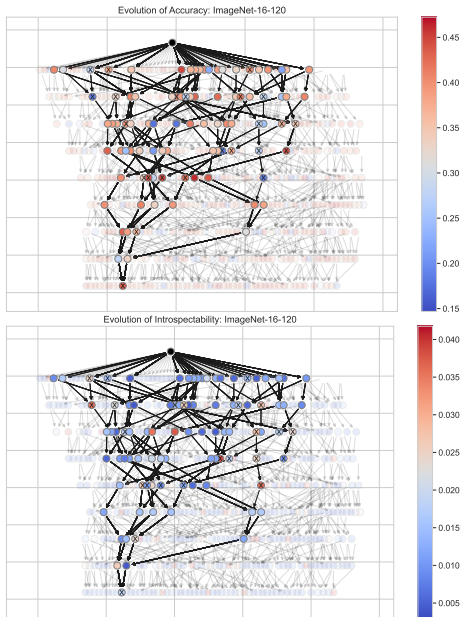


Figure 3. Phylogenetic trees showing the evolution of the population in XNAS on the ImageNet-16-120 task up to the eighth generation. The mating path from the initial population to a solution in the final Pareto front of the search is emphasized. Along the path, parents that were Pareto-optimal within their own generation are marked with an \times . The evolution of accuracy (top) and introspectability (bottom) within the population are shown.

Note that the best accuracy of XNAS on ImageNet-16-120 is on par with the best-performing methods as evaluated in [16]. We plot the Pareto front of every NAS search result and shade in the hypervolume in Figure 2. The visualizations make clear where the multi-objective approach makes

up hypervolume over single-objective (accuracy). Across all tasks, multi-objective covers a larger range of introspectability values. As one would expect, focusing on accuracy tends to cluster the majority of non-dominated solutions in the upper left of the front. The hypervolume of random guessing illustrates why we set the hypervolume reference point to $(0, 1/N_C)$: some solutions manage to achieve high introspectability but are effectively useless since their predictions are no better than random.

As another baseline, introspectability is employed as a *regularization* term. Introspectability is differentiable and in turn, can be used to train models as an auxiliary loss. However, this drastically increases the training computational complexity and memory utilization due to the calculation of pairwise distances and the accumulation of activations. In experiments, this slows down training by several orders of magnitude. Accordingly, the number of search space evaluations is limited. Regularization achieves introspectability scores competitive with the multi-objective approach on MNIST and ImageNet-16-120, but not CIFAR-10. In addition, the achieved accuracy and hypervolume are hindered due to the reduced evaluations. Synergistically, we also evaluate regularization applied to the Pareto front of the multi-objective approach – XNAS is capable of discovering high-accuracy solutions that are predisposed to higher introspectability via the regularization approach. This combination performs best but demands the additional computation.

To understand the evolution process of XNAS, consider the phylogenetic trees shown in Figure 3. It shows the ancestry for a Pareto-optimal solution from the eighth generation with the ImageNet-16-120 task. While most solutions on a given generation’s Pareto front are not directly

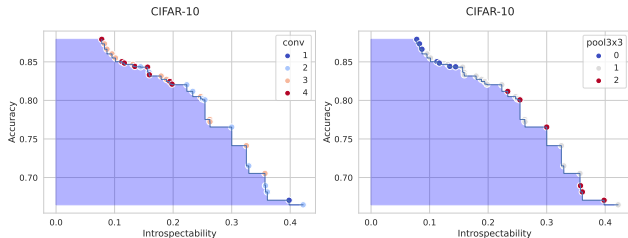


Figure 4. The Pareto front for the CIFAR-10 task with solutions colored by the number of convolutional (left) and pooling (right) layers per cell.

descended from the previous generation’s Pareto front, they typically have many Pareto-optimal ancestors. This suggests that Pareto optimality is mildly heritable, although not enough to ensure direct transmission between generations. In addition, the final Pareto-optimal solution had the second-highest cumulative accuracy at its generation. It is not surprising that its ancestors tended to have above-average accuracy and below-average introspectability.

We conduct an analysis of emerging patterns in the architectures discovered across the Pareto front for each task. The methodology for selecting motifs of interest is described in the supplemental material and is accompanied by the corresponding visualizations. In Figure 4, we elect to visualize a pattern that holds for all tasks but is shown for CIFAR-10. Therein, we observe that more accurate models have fewer pooling layers and more convolutional layers, whereas models with greater introspectability exhibit the opposite tendency. These layer types can be seen as one knob that controls the accuracy-introspectability trade-off. Furthermore, a study of the impact of accuracy and introspectability of the generalization error, convergence speed, and the number of parameters is presented in Appendix J. High-introspectability models have lower generalization error, fewer parameters, and faster training times, whereas high-accuracy models exhibit the inverse trend.

To gain a better qualitative understanding of the introspectability metric, we visualize the activations of the Pareto-optimal solutions of each task. In Figure 5, the solutions of the highest and lowest introspectability are shown for CIFAR-10. The MNIST and ImageNet-16-120 activations are shown in the supplemental material. Within each layer, the activations are normalized using z-score normalization. The activations within each block per class are then averaged for the purpose of visualization. The differences between the highest- and lowest-scoring models are quite apparent; the activation patterns for each class in higher-scoring models have notable variance, whereas they are quite constant in lower-scoring models.

We use principal component analysis (PCA) to visualize the mean activations of the best- and worst-scoring non-dominated models for introspectability on ImageNet-

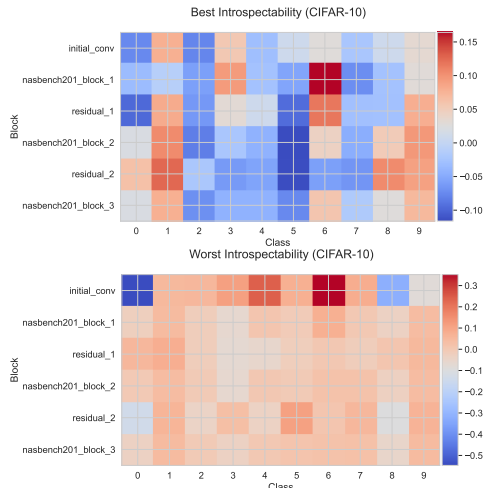


Figure 5. Mean activations heatmap of the model with highest (top) and lowest (bottom) introspectability on the CIFAR-10 task.

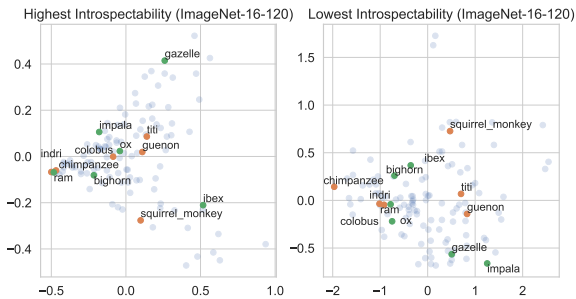


Figure 6. 2D PCA of the mean activations per class from the non-dominated models with highest and lowest introspectability on ImageNet-16-120. Classes with the mutual hypernym “primate” (orange) and “bovid” (green) are emphasized.

16-120, as shown in Figure 6. The labels belonging to the hyponyms of two synsets, primates and bovids, are highlighted for comparison. While neither projection demonstrates complete disentanglement, the higher-introspectability model has more clusters of points within a synset with lower angular distance from the origin.

Introspectability, trustworthiness, and debuggability

Figures 5 and 6 demonstrate that increased class-wise disentanglement is a result of optimizing for introspectability. Here, we exploit this to show that introspectability is a surrogate for improved trustworthiness and debuggability of discovered architectures. Typically, *softmax calibration* is employed to assess the confidence and trustworthiness of predictions. This approach interprets the softmax-activated readout layer outputs of DNN classifiers as probabilities. We propose to use an *activations-based calibration* that XNAS indirectly optimizes for. In activations-based calibration, we 1) collect the mean activations per class from

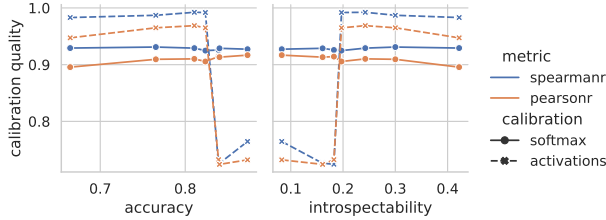


Figure 7. Calibration quality of Pareto-optimal models discovered by XNAS on CIFAR-10. Calibration using activations improves on softmax for introspectability > 0.18 .

training data, 2) collect the activations of the held-out data, 3) compute the cosine distances between the activations of held-out data and the mean activations per class (similar to Eq. (1)), and 4) interpret the distances of the predicted classes as probabilities. To assess calibration quality, we use the Pearson and Spearman rank correlation coefficients of the calibrated probabilities and the corresponding actual accuracy scores at each probability range on a held-out test set². Fig. 7 demonstrates that introspectability estimates calibration quality and outperforms softmax calibration when introspectability > 0.18 . Notably, the calibration quality tapers off rapidly at this point, indicating that class-wise latent representations are no longer as disentangled. This is an important observation of this approach – *DNN trustworthiness is a function of class-wise disentanglement*. This experiment serves as motivation that higher-introspectability models are more conducive to trustworthiness and debuggability, as we will demonstrate.

Identifying mispredictions We explore the effect of introspectability on the ability to identify mispredictions. To do so, low-confidence predictions are isolated according to the distribution of activation calibration scores. The quality of identified mispredictions is then quantified as the increase in accuracy due to removing samples. Figure 8 compares misprediction identification between low- and high-introspectability models on CIFAR-10 – high-introspectability models demonstrate greater improvement owing to superior calibration and trustworthiness.

Debugging data We further demonstrate the improved model comprehensibility to debug data. We mislabel samples at a corruption rate of 20% and assess the ability of models to identify the mislabeled data following the distribution of activation calibration scores. Figure 8 shows that high-introspectability models are better equipped to identify bugs in the data on CIFAR-10, achieving a $\sim 20\%$ higher detection rate at the 20th percentile of scored samples.

Debugging models Further model debugging experiments are included in Appendix K – we identify and repair bugs in models based on pairwise activation distances.

²We use 50 linear bins to estimate these quantities.

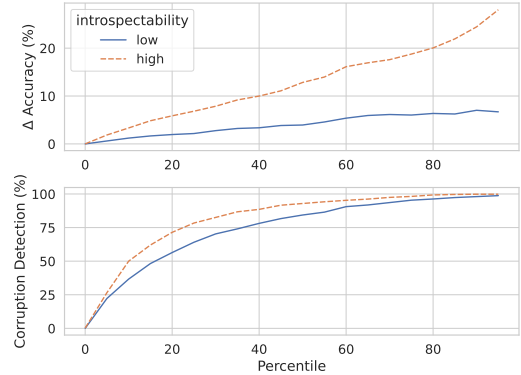


Figure 8. (Top) The change in accuracy due to identified mispredictions as a function of the percentile of sample-wise activation calibration scores. (Bottom) The detection rate of corrupted labels as a function of the percentile of sample-wise activation calibration scores. The results are both on the CIFAR-10 dataset.

5. Discussion

As can be observed in Figure 2, there exists a clear trade-off between the two metrics, accuracy and introspectability. This trade-off is more pronounced as the classification task grows more complex, i.e. in the order of MNIST, CIFAR-10, and ImageNet-16-120. Furthermore, we discussed how this trade-off is influenced by the selection of operators within a cell. Interestingly, the observation of this phenomenon seems to contradict the argument by Rudin et al. that the accuracy-interpretability trade-off is a false dichotomy [42]. That said, our observation is based on models of the same class and derived from the same search space, while their argument is based on a comparison between different model classes.

The introspectability scores we propose are best suited for technical users, as discussed in Section 3.3, and should not be confused for an all-telling quantification of fairness, trust, or reliability. However, the introspectability of models discovered by XNAS has the potential to serve as a requisite criterion before being deployed to users or trusted as a valid model. Furthermore, the introspectability score is designed with simplicity and generality in mind. It can be gamed by an adversary with model-level access, e.g. by adding futile blocks after the final softmax layer, but are zeroed out and bypassed with a skip connection. This should be addressed in later work, ideally on a per-application basis.

There are several routes for improvement of the XNAS framework. Foremost, the efficiency can be greatly increased by using weight-sharing techniques [18, 33], which reduce the evaluation time of offspring. Furthermore, there are uninteresting regions of the Pareto front, depending on the application or end user – NSGA-II can be modified to use reference points of interest to guide the multi-objective search towards more desirable solutions [11].

References

- [1] George Adam and Jonathan Lorraine. Understanding neural architecture search techniques. *CoRR*, abs/1904.00438, 2019. [3](#)
- [2] Peter J. Angeline, Gregory M. Saunders, and Jordan B. Pollack. An evolutionary algorithm that constructs recurrent neural networks. *IEEE Trans. Neural Networks*, 5(1):54–65, 1994. [2](#)
- [3] Prasanna Balaprakash, Michael A. Salim, Thomas D. Uram, Venkat Vishwanath, and Stefan M. Wild. Deephyper: Asynchronous hyperparameter search for deep neural networks. In *25th IEEE International Conference on High Performance Computing, HiPC 2018, Bengaluru, India, December 17-20, 2018*, pages 42–51. IEEE, 2018. [5](#)
- [4] David Bau, Jun-Yan Zhu, Hendrik Strobelt, Àgata Lapedriza, Bolei Zhou, and Antonio Torralba. Understanding the role of individual units in a deep neural network. *Proc. Natl. Acad. Sci. USA*, 117(48):30071–30078, 2020. [24](#)
- [5] James Bergstra, Daniel Yamins, and David D. Cox. Making a science of model search: Hyperparameter optimization in hundreds of dimensions for vision architectures. In *Proceedings of the 30th International Conference on Machine Learning, ICML 2013, Atlanta, GA, USA, 16-21 June 2013*, volume 28 of *JMLR Workshop and Conference Proceedings*, pages 115–123. JMLR.org, 2013. [2](#)
- [6] J. Blank and K. Deb. pymoo: Multi-objective optimization in python. *IEEE Access*, 8:89497–89509, 2020. [5](#)
- [7] Han Cai, Tianyao Chen, Weinan Zhang, Yong Yu, and Jun Wang. Efficient architecture search by network transformation. In Sheila A. McIlraith and Kilian Q. Weinberger, editors, *Proceedings of the Thirty-Second AAAI Conference on Artificial Intelligence*, pages 2787–2794. AAAI Press, 2018. [2](#)
- [8] Patryk Chrabaszcz, Ilya Loshchilov, and Frank Hutter. A downsampled variant of imagenet as an alternative to the CIFAR datasets. *CoRR*, abs/1707.08819, 2017. [13](#)
- [9] K. Deb, A. Pratap, S. Agarwal, and T. Meyarivan. A fast and elitist multiobjective genetic algorithm: NSGA-II. *IEEE Transactions on Evolutionary Computation*, 6(2):182–197, 2002. [2](#), [3](#)
- [10] Kalyanmoy Deb, Karthik Sindhya, and Tatsuya Okabe. Self-adaptive simulated binary crossover for real-parameter optimization. In *Proceedings of the 9th Annual Conference on Genetic and Evolutionary Computation, GECCO '07*, page 1187–1194, New York, NY, USA, 2007. Association for Computing Machinery. [3](#)
- [11] Kalyanmoy Deb and J. Sundar. Reference point based multi-objective optimization using evolutionary algorithms. In *Proceedings of the 8th Annual Conference on Genetic and Evolutionary Computation, GECCO '06*, page 635–642, New York, NY, USA, 2006. Association for Computing Machinery. [8](#)
- [12] Jia Deng, Wei Dong, Richard Socher, Li-Jia Li, Kai Li, and Li Fei-Fei. Imagenet: A large-scale hierarchical image database. In *2009 IEEE Computer Society Conference on Computer Vision and Pattern Recognition (CVPR 2009)*, 20–25 June 2009, Miami, Florida, USA, pages 248–255. IEEE Computer Society, 2009. [4](#)
- [13] Terrance Devries and Graham W. Taylor. Improved regularization of convolutional neural networks with cutout. *CoRR*, abs/1708.04552, 2017. [13](#)
- [14] Tobias Domhan, Jost Tobias Springenberg, and Frank Hutter. Speeding up automatic hyperparameter optimization of deep neural networks by extrapolation of learning curves. In Qiang Yang and Michael J. Wooldridge, editors, *Proceedings of the Twenty-Fourth International Joint Conference on Artificial Intelligence, IJCAI*, pages 3460–3468. AAAI Press, 2015. [2](#)
- [15] Jin-Dong Dong, An-Chieh Cheng, Da-Cheng Juan, Wei Wei, and Min Sun. PPP-net: Platform-aware progressive search for Pareto-optimal neural architectures. In *6th International Conference on Learning Representations, ICLR 2018, Vancouver, BC, Canada, April 30 - May 3, 2018, Workshop Track Proceedings*. OpenReview.net, 2018. [22](#)
- [16] Xuanyi Dong and Yi Yang. Nas-bench-201: Extending the scope of reproducible neural architecture search. In *8th International Conference on Learning Representations, ICLR 2020, Addis Ababa, Ethiopia, April 26-30, 2020*. OpenReview.net, 2020. [3](#), [5](#), [6](#), [13](#)
- [17] Thomas Elsken, Jan Hendrik Metzen, and Frank Hutter. Efficient multi-objective neural architecture search via Lamarckian evolution. In *7th International Conference on Learning Representations, ICLR 2019, New Orleans, LA, USA, May 6-9, 2019*. OpenReview.net, 2019. [2](#)
- [18] Thomas Elsken, Jan Hendrik Metzen, and Frank Hutter. Neural architecture search: A survey. *The Journal of Machine Learning Research*, 20(1):1997–2017, 2019. [1](#), [2](#), [3](#), [8](#)
- [19] Dumitru Erhan, Yoshua Bengio, Aaron Courville, and Pascal Vincent. Visualizing higher-layer features of a deep network. *University of Montreal*, 1341(3):1, 2009. [24](#)
- [20] Carlos M. Fonseca, Luís Paquete, and Manuel López-Ibáñez. An improved dimension-sweep algorithm for the hypervolume indicator. In *IEEE International Conference on Evolutionary Computation, CEC 2006, part of WCCI 2006, Vancouver, BC, Canada, 16-21 July 2006*, pages 1157–1163. IEEE, 2006. [5](#)
- [21] Amirata Ghorbani and James Y. Zou. Neuron shapley: Discovering the responsible neurons. In Hugo Larochelle, Marc’Aurelio Ranzato, Raia Hadsell, Maria-Florina Balcan, and Hsuan-Tien Lin, editors, *Advances in Neural Information Processing Systems 33: Annual Conference on Neural Information Processing Systems 2020, NeurIPS 2020, December 6-12, 2020, virtual*, 2020. [24](#)
- [22] David Gunning. Darpa’s explainable artificial intelligence (xai) program. In *Proceedings of the 24th International Conference on Intelligent User Interfaces, IUI '19*, page ii, New York, NY, USA, 2019. Association for Computing Machinery. [24](#)
- [23] Kaiming He, Xiangyu Zhang, Shaoqing Ren, and Jian Sun. Identity mappings in deep residual networks. In Bastian Leibe, Jiri Matas, Nicu Sebe, and Max Welling, editors, *Computer Vision - ECCV 2016 - 14th European Conference*,

- volume 9908 of *Lecture Notes in Computer Science*, pages 630–645. Springer, 2016. 3
- [24] Irina Higgins, Loïc Matthey, Arka Pal, Christopher Burgess, Xavier Glorot, Matthew Botvinick, Shakir Mohamed, and Alexander Lerchner. beta-vae: Learning basic visual concepts with a constrained variational framework. In *5th International Conference on Learning Representations, ICLR 2017*. OpenReview.net, 2017. 24
- [25] John H. Holland. *Adaptation in Natural and Artificial Systems: An Introductory Analysis with Applications to Biology, Control, and Artificial Intelligence*. The MIT Press, 04 1992. 3
- [26] Chi-Hung Hsu, Shu-Huan Chang, Da-Cheng Juan, Jia-Yu Pan, Yu-Ting Chen, Wei Wei, and Shih-Chieh Chang. MONAS: multi-objective neural architecture search using reinforcement learning. *CoRR*, abs/1806.10332, 2018. 2, 22
- [27] Gao Huang, Zhuang Liu, Laurens van der Maaten, and Kilian Q. Weinberger. Densely connected convolutional networks. In *2017 IEEE Conference on Computer Vision and Pattern Recognition, CVPR 2017, Honolulu, HI, USA, July 21-26, 2017*, pages 2261–2269. IEEE Computer Society, 2017. 3
- [28] Been Kim, Martin Wattenberg, Justin Gilmer, Carrie J. Cai, James Wexler, Fernanda B. Viégas, and Rory Sayres. Interpretability beyond feature attribution: Quantitative testing with concept activation vectors (TCAV). In Jennifer G. Dy and Andreas Krause, editors, *Proceedings of the 35th International Conference on Machine Learning*, volume 80 of *Proceedings of Machine Learning Research*, pages 2673–2682. PMLR, 2018. 24
- [29] Diederik P. Kingma and Max Welling. Auto-encoding variational bayes. In Yoshua Bengio and Yann LeCun, editors, *2nd International Conference on Learning Representations, ICLR 2014, Banff, AB, Canada, April 14-16, 2014, Conference Track Proceedings*, 2014. 24
- [30] Pang Wei Koh and Percy Liang. Understanding black-box predictions via influence functions. In Doina Precup and Yee Whye Teh, editors, *Proceedings of the 34th International Conference on Machine Learning, ICML 2017, Sydney, NSW, Australia, 6-11 August 2017*, volume 70 of *Proceedings of Machine Learning Research*, pages 1885–1894. PMLR, 2017. 24
- [31] Hanxiao Liu, Karen Simonyan, and Yiming Yang. DARTS: differentiable architecture search. In *7th International Conference on Learning Representations, ICLR 2019, New Orleans, LA, USA, May 6-9, 2019*. OpenReview.net, 2019. 2
- [32] Ilya Loshchilov and Frank Hutter. SGDR: stochastic gradient descent with warm restarts. In *5th International Conference on Learning Representations, ICLR 2017, Toulon, France, April 24-26, 2017, Conference Track Proceedings*. OpenReview.net, 2017. 12
- [33] Zhichao Lu, Ian Whalen, Vishnu Boddeti, Yashesh D. Dhebar, Kalyanmoy Deb, Erik D. Goodman, and Wolfgang Banzhaf. NSGA-Net: neural architecture search using multi-objective genetic algorithm. In Anne Auger and Thomas Stützle, editors, *Proceedings of the Genetic and Evolutionary Computation Conference (GECCO)*, pages 419–427. ACM, 2019. 2, 8, 22
- [34] R. T. Marler and J. S. Arora. Survey of multi-objective optimization methods for engineering. *Structural and Multidisciplinary Optimization*, 26(6):369–395, Apr 2004. 2
- [35] Hector Mendoza, Aaron Klein, Matthias Feurer, Jost Tobias Springenberg, and Frank Hutter. Towards automatically-tuned neural networks. In Frank Hutter, Lars Kotthoff, and Joaquin Vanschoren, editors, *Proceedings of the 2016 Workshop on Automatic Machine Learning (AutoML)*, volume 64 of *JMLR Workshop and Conference Proceedings*, pages 58–65. JMLR.org, 2016. 2
- [36] George A Miller. WordNet: a lexical database for English. *Communications of the ACM*, 38(11):39–41, 1995. 4
- [37] Geoffrey F. Miller, Peter M. Todd, and Shailesh U. Hegde. Designing neural networks using genetic algorithms. In J. David Schaffer, editor, *Proceedings of the 3rd International Conference on Genetic Algorithms*, pages 379–384. Morgan Kaufmann, 1989. 2
- [38] Philipp Moritz, Robert Nishihara, Stephanie Wang, Alexey Tumanov, Richard Liaw, Eric Liang, Melih Elibol, Zongheng Yang, William Paul, Michael I. Jordan, and Ion Stoica. Ray: A distributed framework for emerging AI applications. In Andrea C. Arpaci-Dusseau and Geoff Voelker, editors, *13th USENIX Symposium on Operating Systems Design and Implementation*, pages 561–577. USENIX Association, 2018. 2, 5
- [39] Esteban Real, Alok Aggarwal, Yanping Huang, and Quoc V. Le. Regularized evolution for image classifier architecture search. In *The Thirty-Third AAAI Conference on Artificial Intelligence*, pages 4780–4789. AAAI Press, 2019. 1, 2
- [40] Esteban Real, Sherry Moore, Andrew Selle, Saurabh Saxena, Yutaka Leon Suematsu, Jie Tan, Quoc V. Le, and Alexey Kurakin. Large-scale evolution of image classifiers. In Doina Precup and Yee Whye Teh, editors, *Proceedings of the 34th International Conference on Machine Learning*, volume 70 of *Proceedings of Machine Learning Research*, pages 2902–2911. PMLR, 2017. 2
- [41] Bin Xin Ru, Xingchen Wan, Xiaowen Dong, and Michael A. Osborne. Interpretable neural architecture search via bayesian optimisation with weisfeiler-lehman kernels. In *9th International Conference on Learning Representations, ICLR 2021, Virtual Event, Austria, May 3-7, 2021*. OpenReview.net, 2021. 3
- [42] Cynthia Rudin and Joanna Radin. Why are we using black box models in ai when we don’t need to? a lesson from an explainable ai competition. *Harvard Data Science Review*, 1(2), 11 2019. 8
- [43] Kenneth O. Stanley and Risto Miikkulainen. Evolving neural networks through augmenting topologies. *Evolutionary Computation*, 10(2):99–127, 2002. 2
- [44] Tao Wei, Changhu Wang, and Chang Wen Chen. Modularized morphing of deep convolutional neural networks: A graph approach. *IEEE Trans. Computers*, 70(2):305–315, 2021. 2
- [45] Jason Yosinski, Jeff Clune, Anh Mai Nguyen, Thomas J. Fuchs, and Hod Lipson. Understanding neural networks through deep visualization. *CoRR*, abs/1506.06579, 2015. 24

- [46] Quanshi Zhang, Ying Nian Wu, and Song-Chun Zhu. Interpretable convolutional neural networks. In *2018 IEEE Conference on Computer Vision and Pattern Recognition, CVPR 2018, Salt Lake City, UT, USA, June 18-22, 2018*, pages 8827–8836. Computer Vision Foundation / IEEE Computer Society, 2018. [24](#)
- [47] Xinyue Zheng, Peng Wang, Qigang Wang, and Zhongchao Shi. Disentangled neural architecture search. *CoRR*, abs/2009.13266, 2020. [3](#)
- [48] Eckart Zitzler and Lothar Thiele. Multiobjective optimization using evolutionary algorithms - A comparative case study. In A. E. Eiben, Thomas Bäck, Marc Schoenauer, and Hans-Paul Schwefel, editors, *Parallel Problem Solving from Nature - PPSN V, 5th International Conference*, volume 1498 of *Lecture Notes in Computer Science*, pages 292–304. Springer, 1998. [5](#)
- [49] Barret Zoph and Quoc V. Le. Neural architecture search with reinforcement learning. In *5th International Conference on Learning Representations, ICLR 2017, Toulon, France, April 24-26, 2017, Conference Track Proceedings*. OpenReview.net, 2017. [2](#)
- [50] Barret Zoph, Vijay Vasudevan, Jonathon Shlens, and Quoc V. Le. Learning transferable architectures for scalable image recognition. In *2018 IEEE Conference on Computer Vision and Pattern Recognition, CVPR 2018, Salt Lake City, UT, USA, June 18-22, 2018*, pages 8697–8710. Computer Vision Foundation / IEEE Computer Society, 2018. [1](#), [2](#)

Supplemental Material

Contents

1. Introduction	1
2. Background & Related Work	1
3. Proposed Framework: xNAS	3
3.1. Search Space	3
3.2. Search Strategy	3
3.3. Performance Evaluation Strategy	4
3.4. Scaling Up	5
4. Experiments & Results	5
4.1. Setup and Implementation	5
4.2. Metrics	5
4.3. Results	5
5. Discussion	8
A NAS-Bench-201 Overview	12
B Experiment Setup and Hyperparameters	12
C Additional Activation Heat Maps	13
D Additional PCA Visualizations	13
E Analysis of Operator Selection	14
F. Frequentist Analysis of Motifs	15
G Comparing Motifs Across the Pareto Front	16
H Comparing Evolution of Single- and Multi-Objective Search	21
I. Comparing xNAS Accuracy with Related NAS Methods	22
J. Additional Ablation Studies	22
K Model Debugging Experiments	23
L Extended Background	24
A. NAS-Bench-201 Overview	

The NAS-Bench-201 search space is comprised of a macro skeleton and a searched cell. An overview is shown in Figure A1.

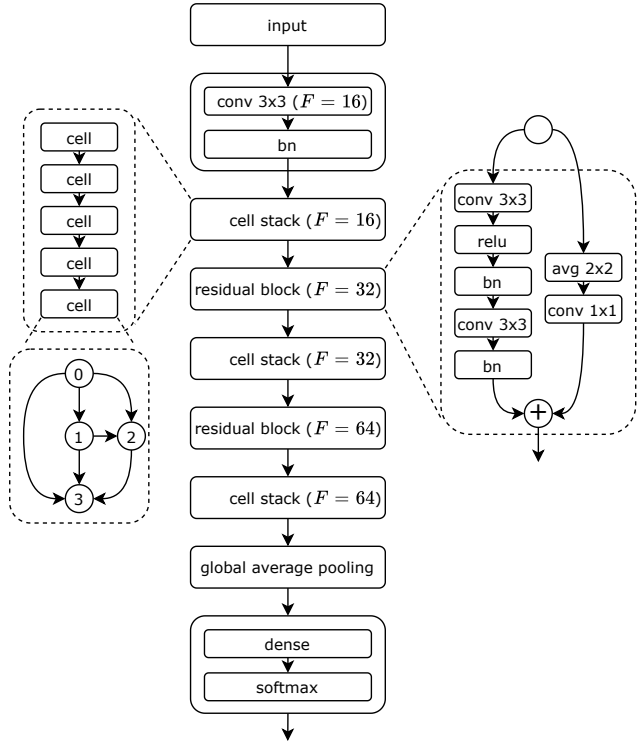


Figure A1. Visualization of the architectures generated by the search space. Note that the first convolutional layer in the main path and the average pooling layer in the shortcut path of each residual block has a stride of 2. conv: 2D convolutional layer. bn: batch normalization. relu: rectified linear (ReLU) activation layer. avg: 2D average pooling layer. F : the number of convolutional filters within each layer of a block.

B. Experiment Setup and Hyperparameters

Setup We use a cosine annealing [32] learning rate schedule to decay the learning rate from 0.1 to 0 at the end of the last epoch. We also take half an epoch to warm up the learning rate from 0 to 0.1 at midway through the first epoch.

Data preprocessing Recall that each raw image \mathcal{X}_i has a height of H pixels, width of W pixels, and C color channels. We first scale the image by 255 to map the input domain from $[0..255] \subset \mathbb{N}_0$ to $[0, 1] \subset \mathbb{R}$. Then, z-score normalization is applied, i.e. the channel-wise mean of the full dataset \mathcal{X} is subtracted from each \mathcal{X}_i and the result of which is divided by the channel-wise standard deviation of \mathcal{X} . The resulting data has channel-wise means of zero and standard deviations of one.

	Hyperparameter	Value
Model Training	Loss	Cross Entropy
	Optimizer	SGD
	Learning Rate (LR)	0.1
	LR Schedule	Cosine Decay
	Nesterov	Yes
	Momentum	0.9
	Weight Decay	0.0005
	Batch Size	512
	Epochs	5*, 12 [†] , 200 [‡]
	Data Normalization	Z-Score (Channel-Wise)
Data Augmentation	See Text	
NSGA-II	Population Size	64
	Sampling	Uniform Random
	Crossover	Simulated Binary $p = 0.9, \eta = 3$
	Mutation	Polynomial $p = 1/6, \eta = 3$

Table B1. Summary of hyperparameters used across each experiment. *MNIST; [†]CIFAR-10; [‡]ImageNet-16-120

Data augmentation We zero-pad the left and right of each image with $\lceil H/8 \rceil$ pixels and the top and bottom of each image with $\lceil W/8 \rceil$ pixels. Then, each image is randomly cropped following a uniform distribution back to shape $H \times W \times C$. Next, the image is flipped horizontally with a probability of 0.5. The final augmentation applied is cutout [13]. Randomly centered rectangular windows with height $2\lceil H/8 \rceil$ and width $2\lceil W/8 \rceil$ are selected to be filled with zeros within the bounds of each image.

We do not allow offspring that have the same architecture as another offspring or a previously evaluated architecture. There are 6 integer variables in the optimization problem, so we set the probability of polynomial mutation per variable to 1/6. Table B1 contains the summary of all hyperparameters used across the experiments.

ImageNet-16-120 The ImageNet-16-120 dataset, originally introduced in [8] and adapted by the NAS-Bench-201 benchmark [16], is a downsampled version of the ImageNet dataset. The dataset facilitates substantially faster experimentation while permitting satisfactory classification results – performance on ImageNet-16-120 has been shown to be indicative of performance across all of ImageNet. Each image in the dataset is resized to 16×16 pixels and only the data for the first 120 classes are retained.

Introspectability Regularizer Introspectability can be used as a regularization term as it is differentiable. We add this as an auxiliary loss term and naively balance the term with cross entropy with a regularizer weight of 0.5 – this bounds introspectability to the range $[0, 1]$. Because we

want to maximize introspectability, we take the cosine similarity instead of the distance. To accumulate activations grouped by classes in TensorFlow, the `tf.scatter_nd` operator is used in implementation. The remaining implementation is straightforward.

C. Additional Activation Heat Maps

To gain a better qualitative understanding of the introspectability metric, we visualize the activations of the Pareto-optimal solutions of each task. In Figure C2, the solutions of the highest and lowest introspectability are shown for MNIST and ImageNet-16-120 (see main text for CIFAR-10). Within each layer, the activations are normalized using z-score normalization. The activations within each block per class are then averaged for the purpose of visualization. The differences between the highest- and lowest-scoring models are quite apparent; the activation patterns for each class in higher-scoring models have notable variance, whereas they are quite constant in lower-scoring models. The heat maps are best viewed digitally.

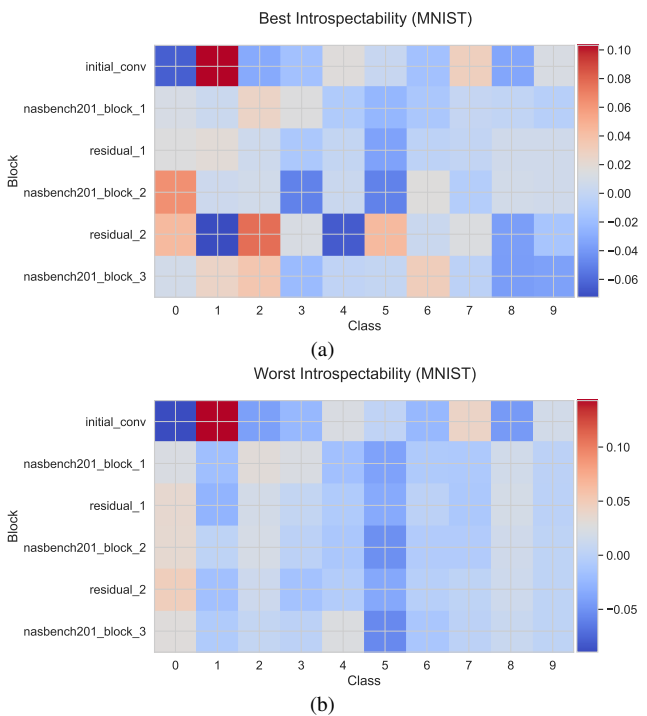


Figure C1. Mean activations heatmap of the models with (a) highest and (b) lowest introspectability on the MNIST task.

D. Additional PCA Visualizations

The remaining 2D PCA activation visualizations are shown for the MNIST and CIFAR-10 tasks in Figure D1 and Figure D2, respectively. For MNIST, there is little dis-

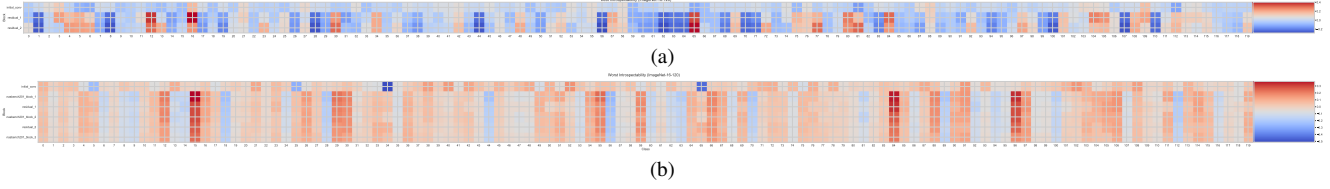


Figure C2. Mean activations heatmap of the model with highest introspectability on the ImageNet-16-120 task.

cernible difference between the models with highest and lowest introspectability – this is expected as the difference between these introspectability scores is small (see the main text). For CIFAR-10, an apparent difference between the two models can be observed; the spread of points about the origin is more Gaussian with the higher-scoring model, which, empirically, should indicate a greater mean cosine distance between class representations. It is important to recall that the PCA projection eliminates thousands of dimensions used to represent activations. Naturally, this causes small changes in introspectability to be less apparent in visualizations.

E. Analysis of Operator Selection

We show the operator-level normalized frequencies selected in the Pareto-optimal solutions of each task in Tables E1-E3. The 3x3 convolutions are most popular across all tasks, followed by either 3x3 average pooling or “zeroize” operators. The skip-connect and 1x1 convolutions are least frequent among these solutions.

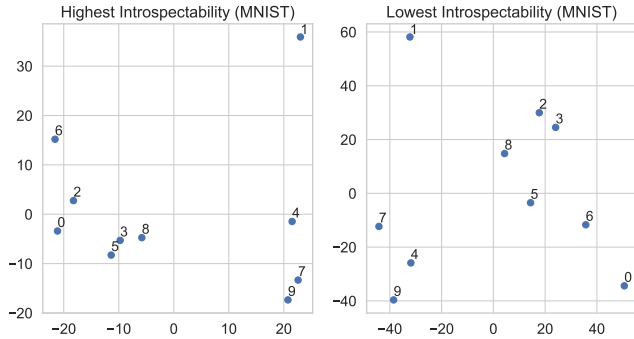


Figure D1. 2D PCA of the mean activations per class from the non-dominated models with highest and lowest introspectability on MNIST.

Operation	Normalized Frequency
3x3 Conv2D	0.51515
3x3 AvgPool2D	0.16667
Zeroize	0.16667
1x1 Conv2D	0.09091
Skip-Connect	0.06061

Table E1. Frequency of operations of solutions in the Pareto front (normalized by total cell operations across the Pareto front models) on the MNIST task

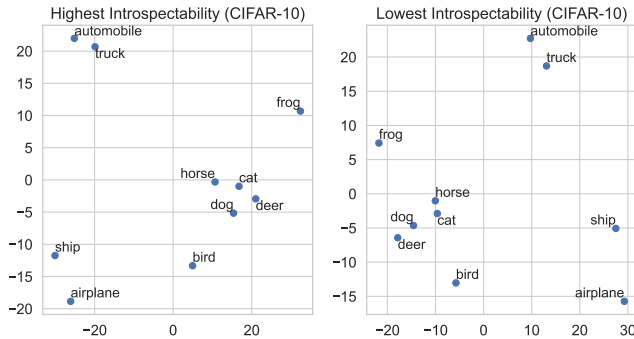


Figure D2. 2D PCA of the mean activations per class from the non-dominated models with highest and lowest introspectability on CIFAR-10.

Operation	Normalized Frequency
3x3 Conv2D	0.44444
Zeroize	0.24306
3x3 AvgPool2D	0.19097
Skip-Connect	0.06250
1x1 Conv2D	0.05903

Table E2. Frequency of operations of solutions in the Pareto front (normalized by total cell operations across the Pareto front models) on the CIFAR-10 task

Operation	Normalized Frequency
3x3 Conv2D	0.48039
3x3 AvgPool2D	0.21078
Zeroize	0.10784
Skip-Connect	0.10784
1x1 Conv2D	0.09314

Table E3. Frequency of operations of solutions in the Pareto front (normalized by total cell operations across the Pareto front models) on the ImageNet-16-120 task

F. Frequentist Analysis of Motifs

We conduct analysis of the most common motifs across the Pareto-optimal solutions of each task, as shown in Tables F1-F3. Recall that the integer-coded cells are encoded as follows:

- 0: 3x3 Conv2D
- 1: 1x1 Conv2D
- 2: 3x3 AvgPool2D
- 3: Zeroize
- 4: Skip-Connect

We also use an asterisk (*) to match any operator. Within each table, the encodings of sizes 1 through 5 are shown alongside its normalized frequency of that size. Motifs of size 6 are not shown as we do not evaluate duplicate architectures (other than isomorphisms). The most common motifs reflect the operator frequencies discussed in the previous section. Interestingly, >67% of the Pareto-optimal solutions of each task all have a common motif of size 1, and >45% a common motif of size 2. This suggests that certain cell topologies exhibit inductive biases specific to the task.

Size	Normalized Frequency	Encoding
1	0.81818	[0 * * * * *]
2	0.45455	[0 * * * 3 *]
2	0.45455	[0 * 0 * * *]
2	0.45455	[0 * * * * 0]
2	0.45455	[* * 0 * * 0]
3	0.36364	[0 * 0 * * 0]
4	0.27273	[0 * 0 4 * 0]
5	0.18182	[0 0 0 4 * 0]
5	0.18182	[0 * 0 4 3 0]

Table F1. Frequency of encodings of solutions in the Pareto front (normalized by the number of Pareto-optimal solutions) on the MNIST task. The top motif (motifs if tied frequency) for each size is shown only

Size	Normalized Frequency	Encoding
1	0.70833	[* * * * 3 *]
2	0.50000	[* * * * 3 0]
3	0.29167	[0 * 0 * 3 *]
3	0.29167	[* * 0 * 3 0]
4	0.18750	[0 * 0 * 3 0]
5	0.08333	[0 * 0 1 3 0]

Table F2. Frequency of encodings of solutions in the Pareto front (normalized by the number of Pareto-optimal solutions) on the CIFAR-10 task. The top motif (motifs if tied frequency) for each size is shown only

Size	Normalized Frequency	Encoding
1	0.67647	[* 0 * * * *]
2	0.47059	[* 0 * * * 0]
3	0.23529	[* 0 * 0 * 0]
4	0.11765	[2 0 * 1 * 0]
4	0.11765	[* 0 * 0 0 0]
4	0.11765	[0 0 * * 0 0]
4	0.11765	[0 0 * 0 * 0]
4	0.11765	[0 * * 0 0 0]
5	0.05882	[3 0 2 2 * 3]
5	0.05882	[2 0 1 1 * 0]
5	0.05882	[2 0 * 1 4 0]
5	0.05882	[2 0 4 0 0 *]
5	0.05882	[2 0 * 0 0 0]

Table F3. Frequency of encodings of solutions in the Pareto front (normalized by the number of Pareto-optimal solutions) on the ImageNet-16-120 task. The top motif (motifs if tied frequency, up to 5) for each size is shown only

G. Comparing Motifs Across the Pareto Front

Motif Discovery

1. Assemble the following data into a tabular structure: architecture encoding, accuracy, and introspectability for the Pareto front of the solutions
2. Sort the data by accuracy and then introspectability which results in data with ascending accuracy and descending introspectability
3. Record the count of each block for each architecture encoding
4. For each architecture encoding in the sorted data, enumerate all applicable motifs of size 1 to 5 (motifs of size 6 cannot exist as architectures are not evaluated multiple times). For example, some architecture encoding $[a, b, c, d, e, f]$ has $\sum_{k=1}^5 \binom{6}{k}$ motifs, e.g. $[a, *, *, *, e, *]$ and $[*, b, c, *, *, f]$ but not, say, $[*, b, c, *, *, e]$. This is nearly equivalent to its power set minus \emptyset and the original sequence. An asterisk here implies a match with any other operator, and thus allows for the comparison of motifs between different architectures
5. For each motif, compute the absolute value of the Spearman rank correlation coefficient between the ranks of the solutions in the sorted data and whether each solution has the motif. If applicable, the count of the operator is used instead of a simple indicator flag.

The intuition here is that we discover interesting architectures that demonstrably are favored more in one part of the Pareto front than another, e.g. the high-accuracy vs. high-introspectability regions

6. In addition to each motif having a correlation score, we also record the support (the number of solutions with the motif) and the motif size
7. Compute the Pareto front of the scored motifs (the costs being the correlation score, the support and the motif size) to identify the most salient motifs. We heuristically eliminate motifs that have support less than 3 or correlation less than 0.2

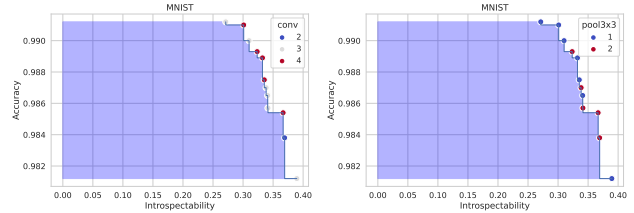


Figure G1. The Pareto front for the MNIST task with solutions colored by the number of convolutional (left) and pooling (right) layers.

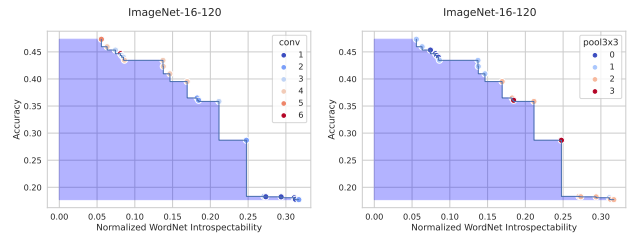


Figure G2. The Pareto front for the ImageNet-16-120 task with solutions colored by the number of convolutional (left) and pooling (right) layers.

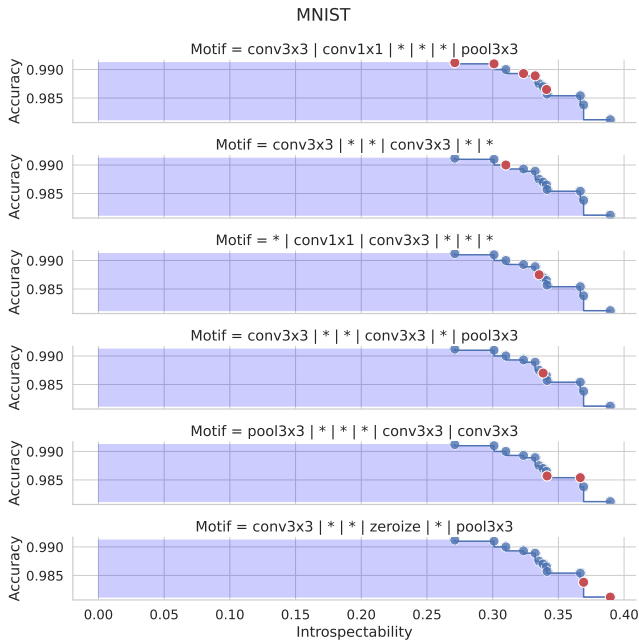


Figure G3. All discovered motifs among the Pareto optimal solutions on the MNIST task. See text for description of the motif discovery process. Each red solution indicates that its architecture has the motif shown in the sub-plot title. The remaining solutions are shown in blue. For the N/A plot, none of the discovered motifs apply to the architecture.

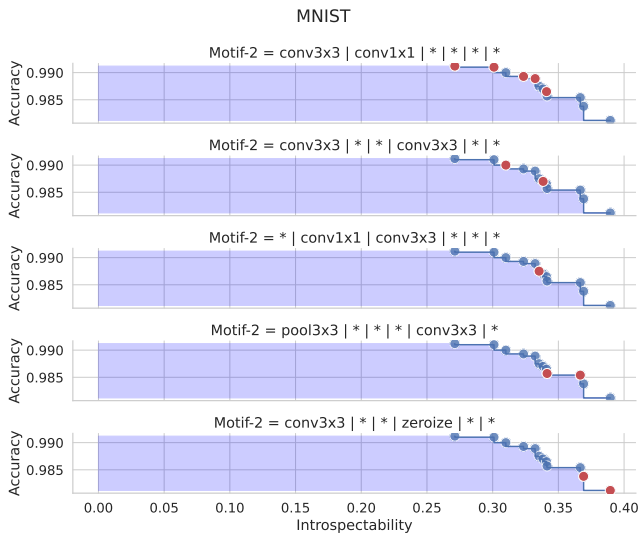


Figure G4. Discovered motifs of size 2 among the Pareto optimal solutions on the MNIST task. See text for description of the motif discovery process. Each red solution indicates that its architecture has the motif shown in the sub-plot title. The remaining solutions are shown in blue. For the N/A plot, none of the discovered motifs apply to the architecture.

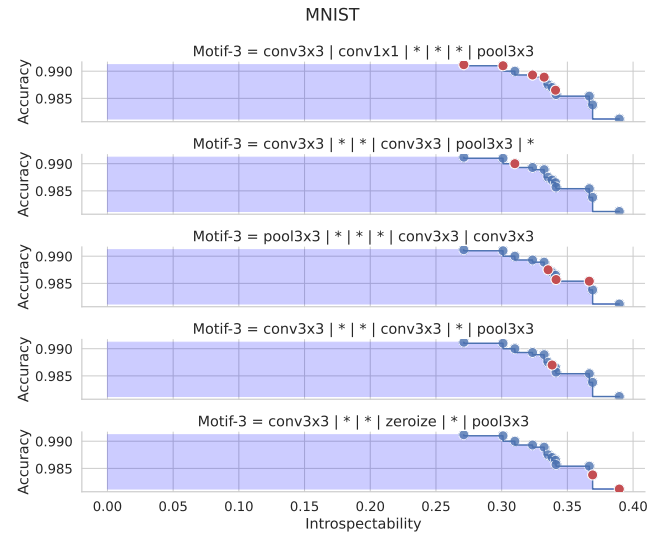


Figure G5. Discovered motifs of size 3 among the Pareto optimal solutions on the MNIST task. See text for description of the motif discovery process. Each red solution indicates that its architecture has the motif shown in the sub-plot title. The remaining solutions are shown in blue. For the N/A plot, none of the discovered motifs apply to the architecture.

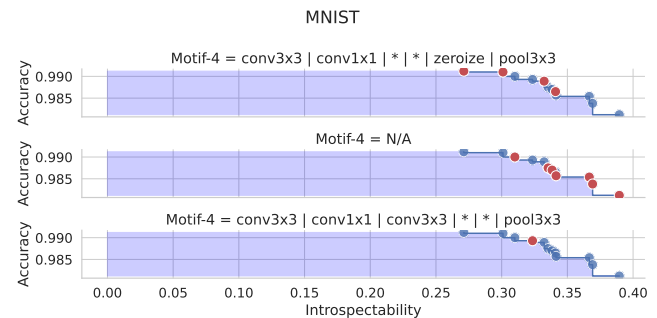


Figure G6. Discovered motifs of size 4 among the Pareto optimal solutions on the MNIST task. See text for description of the motif discovery process. Each red solution indicates that its architecture has the motif shown in the sub-plot title. The remaining solutions are shown in blue. For the N/A plot, none of the discovered motifs apply to the architecture.

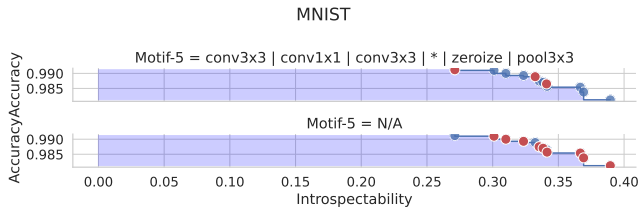


Figure G7. Discovered motifs of size 5 among the Pareto optimal solutions on the MNIST task. See text for description of the motif discovery process. Each red solution indicates that its architecture has the motif shown in the sub-plot title. The remaining solutions are shown in blue. For the N/A plot, none of the discovered motifs apply to the architecture.

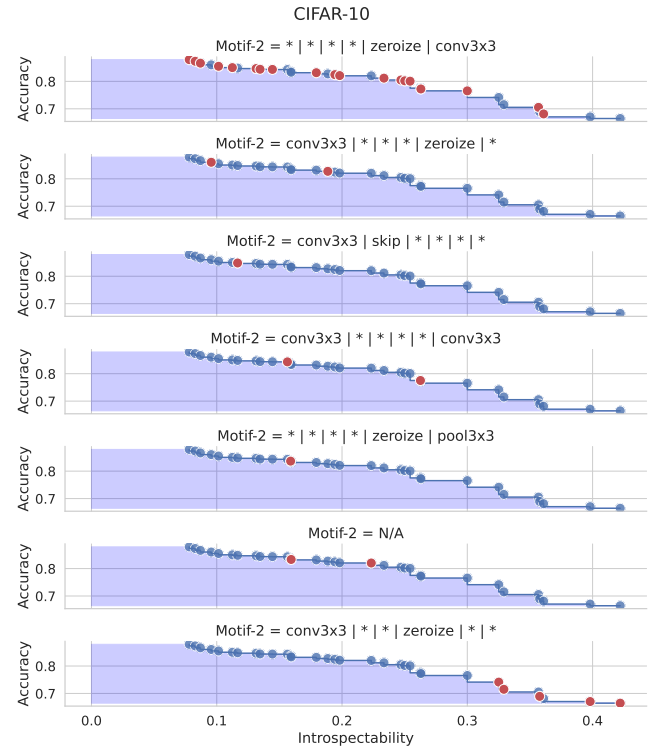


Figure G9. Discovered motifs of size 2 among the Pareto optimal solutions on the CIFAR-10 task. See text for description of the motif discovery process. Each red solution indicates that its architecture has the motif shown in the sub-plot title. The remaining solutions are shown in blue. For the N/A plot, none of the discovered motifs apply to the architecture.

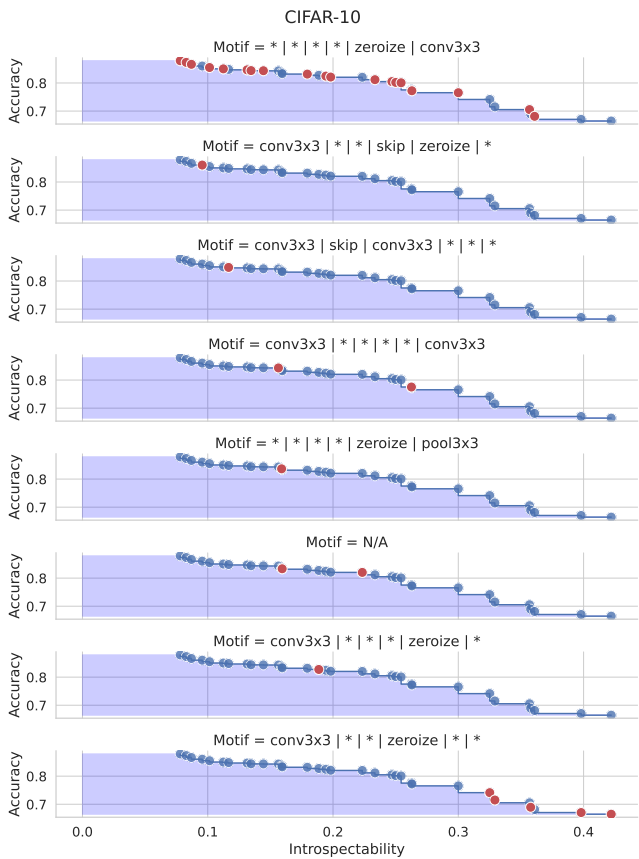


Figure G8. All discovered motifs among the Pareto optimal solutions on the CIFAR-10 task. See text for description of the motif discovery process. Each red solution indicates that its architecture has the motif shown in the sub-plot title. The remaining solutions are shown in blue. For the N/A plot, none of the discovered motifs apply to the architecture.

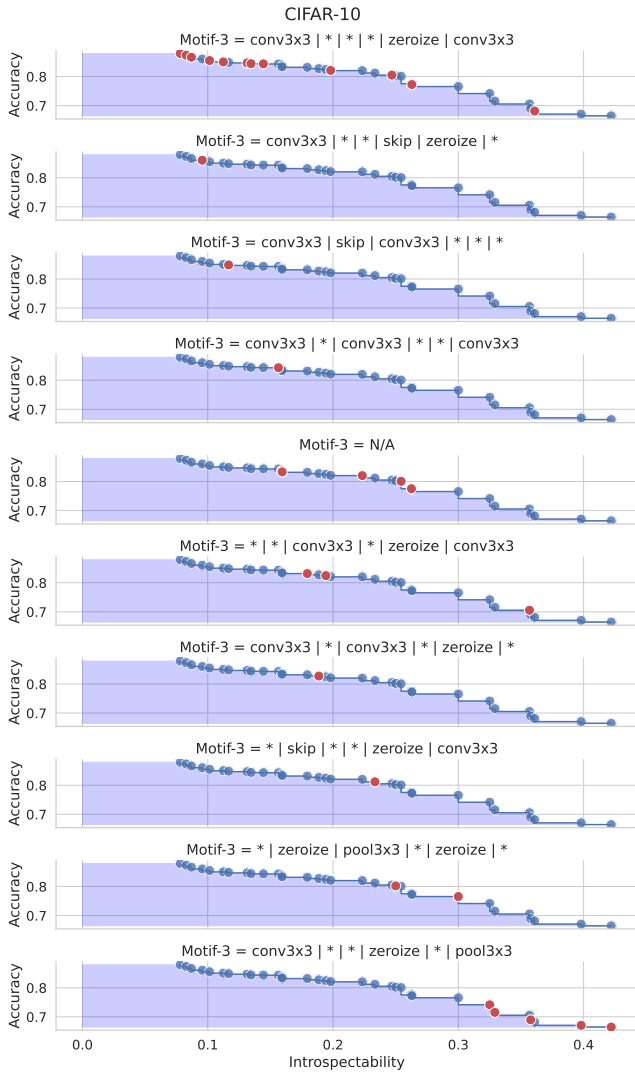


Figure G10. Discovered motifs of size 3 among the Pareto optimal solutions on the CIFAR-10 task. See text for description of the motif discovery process. Each red solution indicates that its architecture has the motif shown in the sub-plot title. The remaining solutions are shown in blue. For the N/A plot, none of the discovered motifs apply to the architecture.

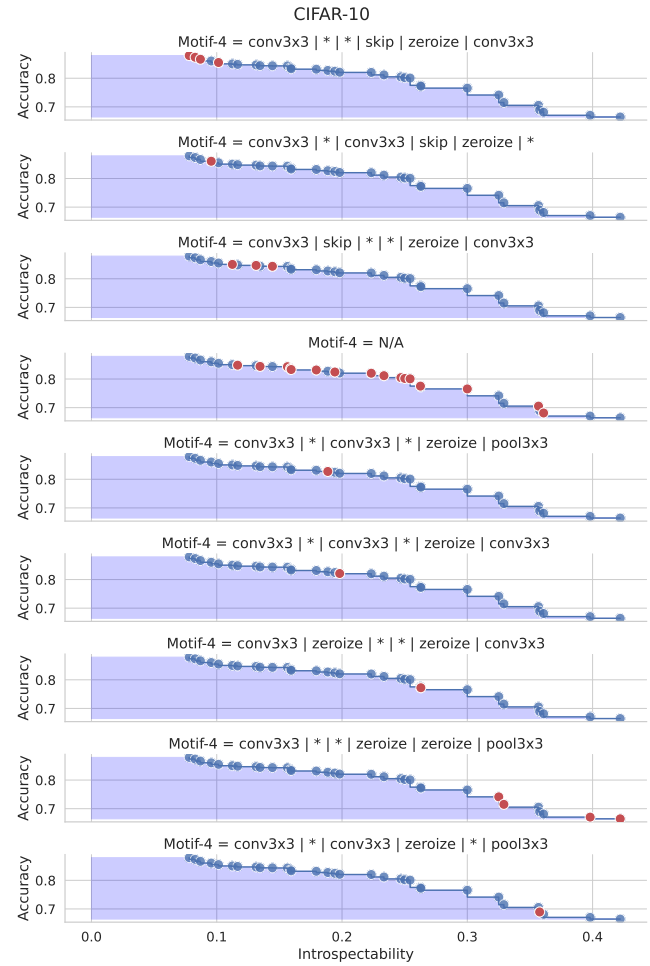


Figure G11. Discovered motifs of size 4 among the Pareto optimal solutions on the CIFAR-10 task. See text for description of the motif discovery process. Each red solution indicates that its architecture has the motif shown in the sub-plot title. The remaining solutions are shown in blue. For the N/A plot, none of the discovered motifs apply to the architecture.

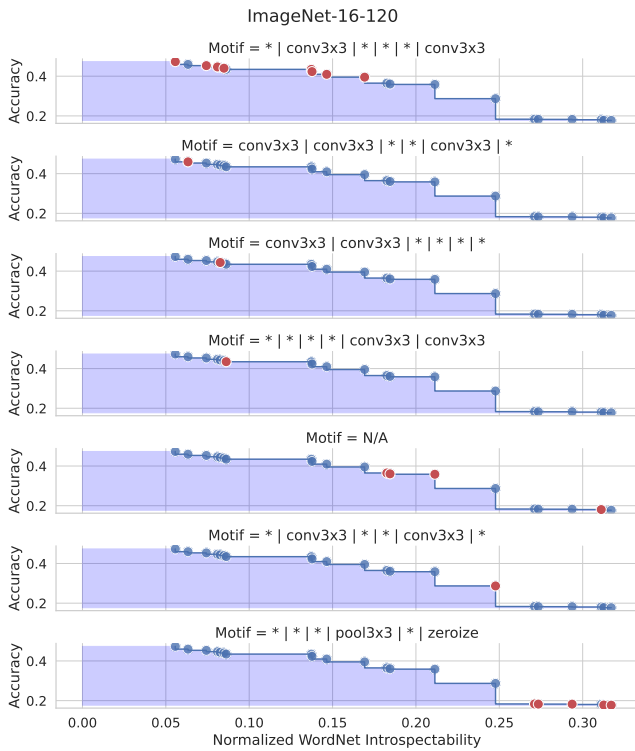


Figure G12. All discovered motifs among the Pareto optimal solutions on the ImageNet-16-120 task. See text for description of the motif discovery process. Each red solution indicates that its architecture has the motif shown in the sub-plot title. The remaining solutions are shown in blue. For the N/A plot, none of the discovered motifs apply to the architecture.

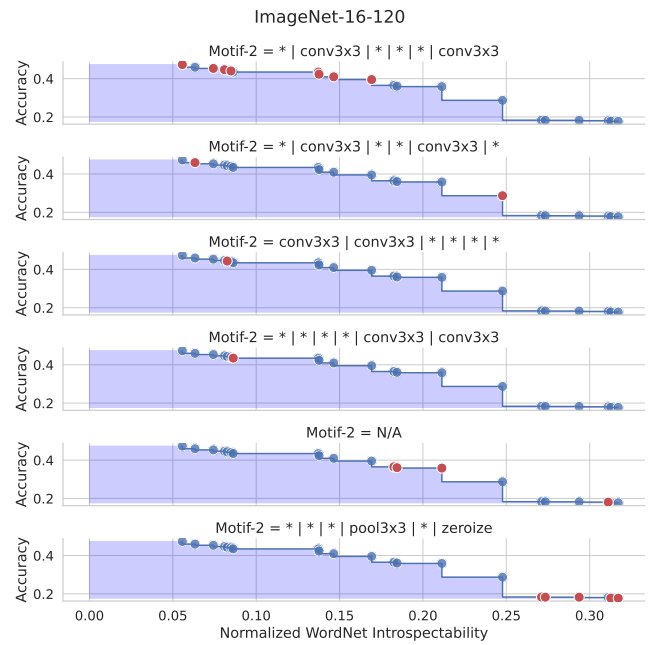


Figure G13. Discovered motifs of size 2 among the Pareto optimal solutions on the ImageNet-16-120 task. See text for description of the motif discovery process. Each red solution indicates that its architecture has the motif shown in the sub-plot title. The remaining solutions are shown in blue. For the N/A plot, none of the discovered motifs apply to the architecture.

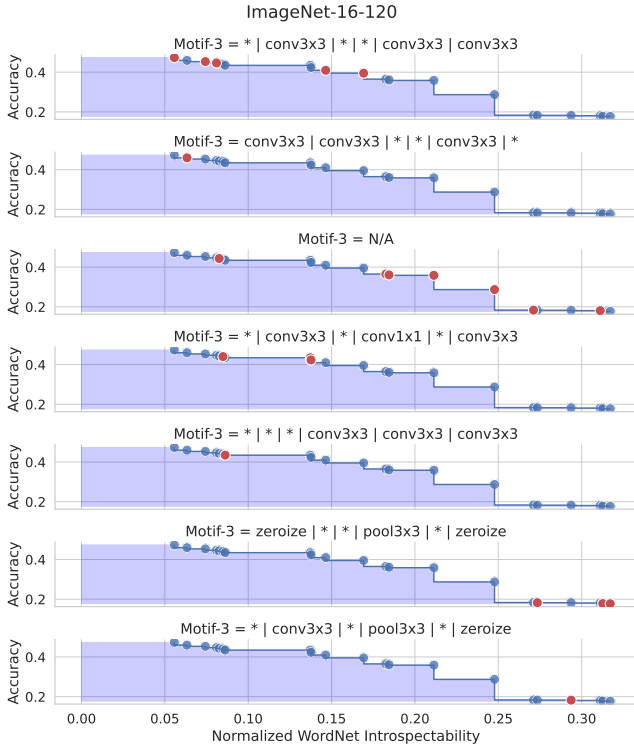


Figure G14. Discovered motifs of size 3 among the Pareto optimal solutions on the ImageNet-16-120 task. See text for description of the motif discovery process. Each red solution indicates that its architecture has the motif shown in the sub-plot title. The remaining solutions are shown in blue. For the N/A plot, none of the discovered motifs apply to the architecture.

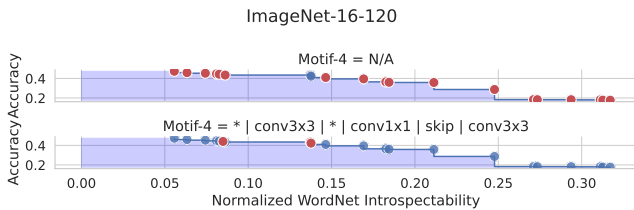


Figure G15. Discovered motifs of size 4 among the Pareto optimal solutions on the ImageNet-16-120 task. See text for description of the motif discovery process. Each red solution indicates that its architecture has the motif shown in the sub-plot title. The remaining solutions are shown in blue. For the N/A plot, none of the discovered motifs apply to the architecture.

H. Comparing Evolution of Single- and Multi-Objective Search

We illustrate the evolution of accuracy and introspectability of the models on the Pareto front over each generation in Figure H1-Figure H3. Each figure contrasts single-objective with multi-objective optimization to better understand the benefit of NSGA-II in our framework. Note

that we do not expect a strict increase in each objective at each generation, which would be expected for population-level statistics, as opposed to statistics within the Pareto front. With single-objective optimization, we can observe that solutions with higher introspectability tend to lie beyond the 95% confidence interval. This indicates fluke solutions, whereas multi-objective more confidently produces higher-introspectability solutions.

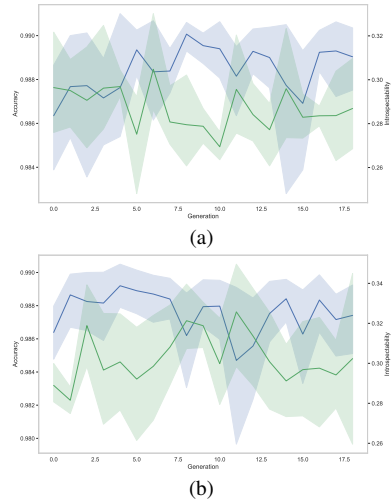


Figure H1. The mean accuracy (blue) and introspectability (green) of the Pareto front solutions each generation on the MNIST task. (a) single-objective; (b) multi-objective. The shaded region indicates the 95% confidence interval of solutions at each generation.

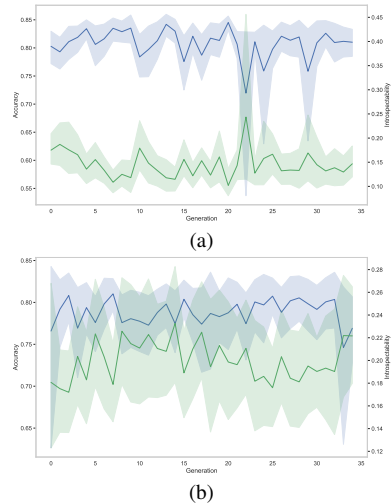


Figure H2. The mean accuracy (blue) and introspectability (green) of the Pareto front solutions each generation on the CIFAR-10 task. (a) single-objective; (b) multi-objective. The shaded region indicates the 95% confidence interval of solutions at each generation.

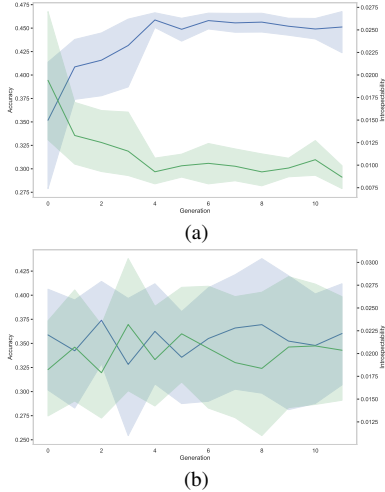


Figure H3. The mean accuracy (blue) and introspectability (green) of the Pareto front solutions each generation on the ImageNet-16-120 task. (a) single-objective; (b) multi-objective. The shaded region indicates the 95% confidence interval of solutions at each generation.

I. Comparing XNAS Accuracy with Related NAS Methods

We compare XNAS to other multi-objective approaches on the CIFAR-10 task. Building on the collected results and approach from [33], we take the architecture with the best accuracy and increase the number of filters by a factor of four. We then perform full training on the CIFAR-10 dataset for 200 epochs. The comparison of results and methods is shown in Table II. While XNAS does not achieve the best accuracy (nor was this the objective of this research), the result is still competitive, especially considering the trade-off between accuracy and introspectability.

Method	Error	Other Objective	Compute
PPP-Net [15]	4.36%	FLOPs, # parameters, or inference time	Nvidia Titan X
MONAS [26]	4.34%	Power	Nvidia 1080 Ti
NSGA-Net [33]	3.85%	FLOPs	Nvidia 1080 Ti 8 GPU Days
XNAS	4.45%	Introspectability	Nvidia Tesla P100 6 GPU Days

Table II. Multi-objective methods for CIFAR-10 (best accuracy for each method). Table adapted from [33]

J. Additional Ablation Studies

We perform additional studies to understand the relationships between the objectives, accuracy and introspectabil-

ity, and the generalization error, number of parameters, and training speed of architectures. Figure J4 demonstrates that introspectability and accuracy have an inverse relationship on the generalization error – this error increases with high-accuracy models and decreases with high-introspectability models. Likewise, the trend can be observed with the number of parameters and training speed as shown in Figures J5 and J6, respectively. These figures follow a similar trend as the number of parameters correlates with the number of FLOPs and thus the training time. As discussed in Section 4.4 of the main text, high-introspectability networks tend to have a more pooling layers whereas high-accuracy networks have more convolutional layers. This helps to explain the trends observed in the number of parameters. A takeaway from this analysis is that the trade-off between accuracy and introspectability also implies a trade-off in parameters (and FLOPs), training time, and generalization error.

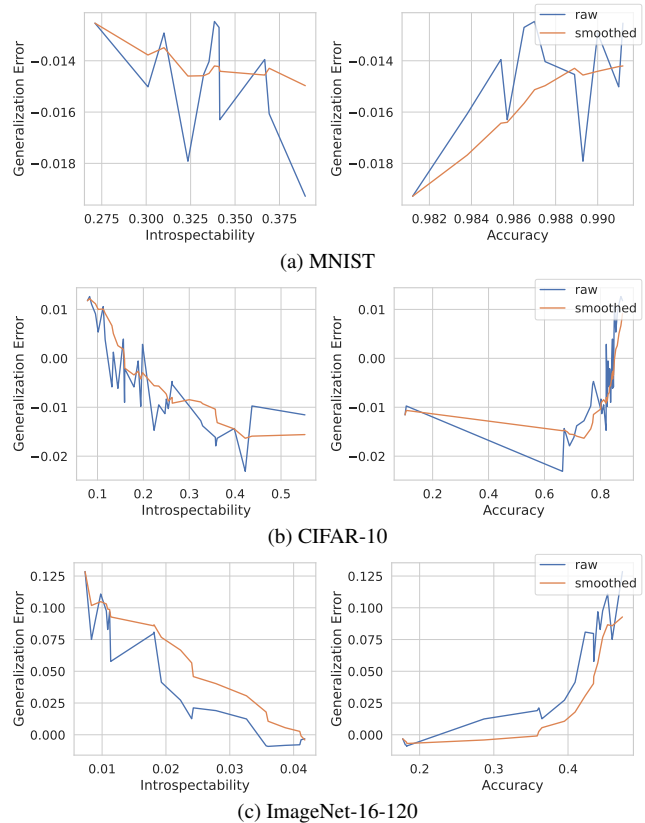


Figure J4. The effect of introspectability and accuracy on generalization error across the tasks.

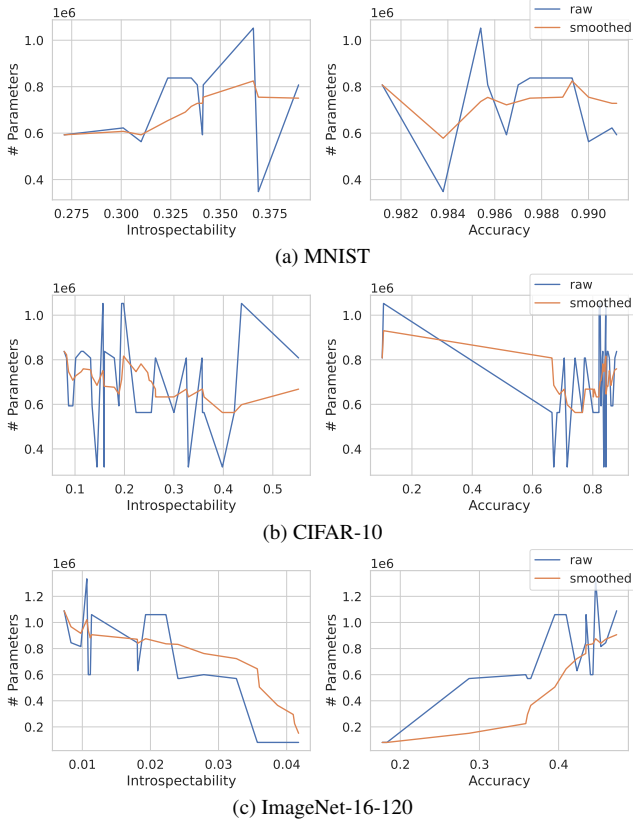


Figure J5. The effect of introspectability and accuracy on the number of parameters across the tasks.

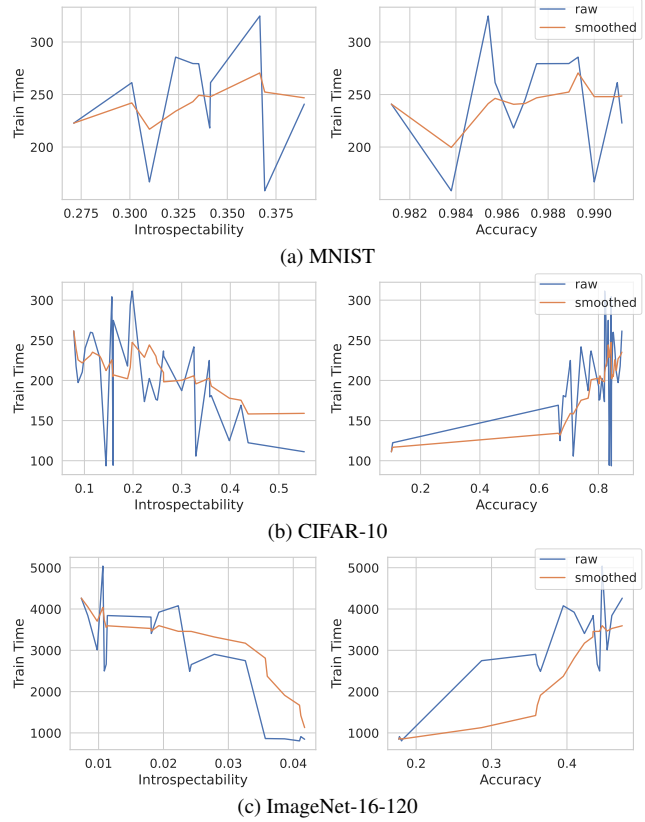


Figure J6. The effect of introspectability and accuracy on the training speed across the tasks.

K. Model Debugging Experiments

Here, we study the ability of our activations calibration approach to correct bugs in models. We first demonstrate that there is a strong connection between the pairwise activation distances used in the formulation of introspectability and the ground truth confusion matrix. To make this comparison, the pairwise distances are negated as disentanglement (separation) between class representations is posited to correlate with confounding. Since the distance between the activations of a class and itself is 0, ideally, the distance between such and the activations of other classes is maximized. There is no information about ground truth available in computing pairwise distances, i.e. the computation is symmetrical and unconditioned. In turn, we compare this information to a confusion matrix folded along the diagonal. This means that element $x_{i,j}, i \neq j$ in the folded confusion matrix is equivalent to the sum $x_{i,j} + x_{j,i}$ in the original confusion matrix. On a higher level, each element $x_{i,j}$ is either the number of true positives for a class (when considering the diagonal), or the support of class i being predicted when class j were true and the support of the converse. To support this, we measure the correlation between the negated pairwise activation distances and the folded ground truth

confusion matrix across Pareto optimal models trained on CIFAR-10. High-introspectability models achieve a correlation of $\rho = 0.85$ while low-introspectability models achieve a correlation of $\rho = 0.59$. With this motivation, we demonstrate how model bugs can be identified and corrected in the following case study.

Case Study: Bug Identification and Correction Figure K7 demonstrates for a random higher-introspectability model trained on CIFAR-10 that there is strong correlation between the negated pairwise activation distances and the ground truth confusion matrix folded along the diagonal ($\rho = 0.81$). Noticeably, the model confounds the classes 3 and 5, which is reflected in the pairwise activations as the smallest distance (largest negated distance).

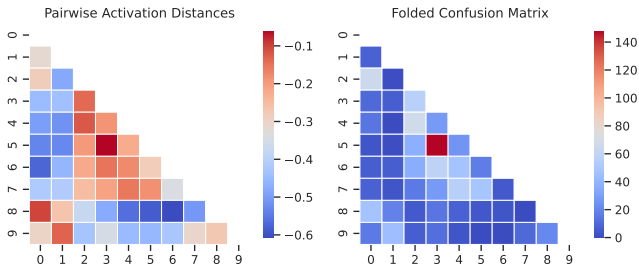


Figure K7. Heat maps of (left) the negated pairwise activation distances as part of the introspectability computation, and (right) the ground truth confusion matrix folded along the diagonal. The heat maps are shown for a random model trained on CIFAR-10. As can be seen, the model confounds the classes 3 and 5, which is reflected in the distance between activations.

With the bug in the model identified, we formulate a strategy to mitigate the issue. The key of our approach is to push the representations of classes 3 and 5 apart in order to reduce the confounding of one another. We accomplish this by using the introspectability regularizer approach with pairwise coefficients. The generalization of this to arbitrary pairs is formalized in Eq. (5).

$$\text{Introspectability}_{\text{reg}}(\mathcal{M}, \mathfrak{X}) = \frac{-1}{\binom{N_C}{2}} \sum_{c=1}^{N_C} \sum_{k=c+1}^{N_C} D(\bar{\Phi}^{(c)}, \bar{\Phi}^{(k)}) \times \omega_{i,j} \quad (5)$$

where $\omega_{i,j}$ is a weight for each class pair (i, j) . With every $\omega_{i,j} = 1$ this is equivalent to the untargeted introspectability regularizer. If the aim is to target all confounded predictions, one can set all $\omega_{i,j}$ proportionally to the pairwise activation distances (or folded confusion matrix). However, we target a single pair in this case study. In our experiment, the model is trained with the regularization term for an additional 5 epochs, a learning rate of 0.001, $\omega_{3,5} = 25$, and all other $\omega_{i,j} = 1$. The results are visualized in Figure K8.

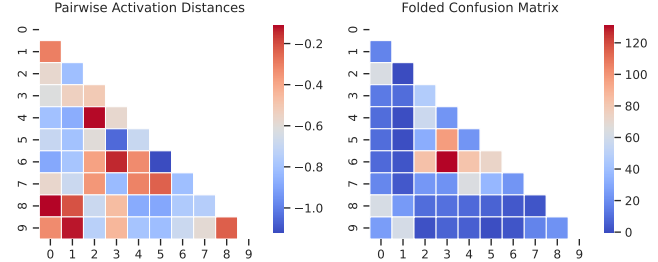


Figure K8. Heat maps after the correction procedure is run of (left) the negated pairwise activation distances as part of the introspectability computation, and (right) the ground truth confusion matrix folded along the diagonal. Note the difference in color scale from Figure K7.

The approach is stronger in identifying bugs than mitigating them, although there is improvement without significant degradation of accuracy ($\pm 0.6\%$ across 10 trials). We leave the tuning of hyperparameters and alternative weighting schemes to future exploration.

L. Extended Background

DNN Inspection within Explainable AI (XAI) The opaque nature of deep neural networks (DNNs) has ultimately led to the sub-field of explainable AI (XAI) [22], which was denominated in 2016 by DARPA, although relevant work predates this by years. Relevant to the subject matter of this work are XAI methods of DNN inspection. This suite of methods enables the debugging of model behavior, the detection of dataset errors, and the development of adversarial attacks. The authors of [30] scale influence functions, a robust statistics method, to DNNs to understand the effect of training points on a prediction. DNN visualization tools have been proposed to provide qualitative modes of analysis. Notably, [19, 45] provide tools for visualizations by gradient ascent, deconvolution for highlighting input images, and discovering preferred input patterns for each class. Probing-based methods aim to qualify the role of DNN internal elements (neurons, latent representations, etc.). In [4, 28], methods are proposed to relate DNN internals to semantic concepts, such as textures, shapes, colors, or even people. Another approach introduced in [21] is to use Shapley values from game theory to quantify the influence each neuron has on overall DNN error.

More related to our work are those related to disentanglement, i.e. the separation of concept- or class-relevant information in a network. For instance, [46] proposes the learning of interpretable CNN filters by coercing feature maps to resemble hand-crafted templates. Moreover, the variational autoencoder (VAE) [29] has been extended to produce a disentangled latent space by regularizing the bottleneck layer [24]. In contrast, we optimize for DNNs with disentangled internal representations of classes without ex-

explicit constraints on the loss, modifications to the architecture, or hand-crafted activation patterns. This also allows for the use of non-differentiable objectives.